Anomalously high heat flow regions beneath the Transantarctic Mountains and Wilkes Subglacial Basin in East Antarctica inferred from Curie depth

Maximilian Lowe[1], Ben R Mather[2], Christopher Green[3], Tom A. Jordan[1], Jörg Ebbing[4], and Robert David Larter[1]

[1]British Antarctic Survey
[2]The University of Sydney
[3]University of Leeds
[4]Kiel University

November 22, 2022

Abstract

The Transantarctic Mountains (TAM) separate the warmer lithosphere of the West Antarctic rift system and the colder East Antarctic craton. Low velocity zones beneath the TAM imaged in recent seismological studies have been interpreted as warm low-density mantle material, suggesting a strong contribution of thermal support to the uplift of the TAM. We present new Curie Depth Point (CDP) and geothermal heat flow (GHF) maps of the northern TAM and adjacent Wilkes Subglacial Basin (WSB) based on high resolution magnetic airborne measurements. We find shallow CDP and high GHF, beneath the northern TAM reinforcing the idea of thermal support of the topography of the mountain range. Additionally, locally high GHF is observed in the Central Basin of the WSB and the Rennick Graben, which has not been resolved previously, while the broader WSB show lower GHF. Across the study area the GHF values range from 30 to 110 mW/m^2. Lastly, we compare our CDP estimates to recent Moho depth estimates and our GHF estimates to sparse in situ GHF measurements as well as to existing continent-wide GHF estimates, which shows closed agreement to previous seismic estimates.

Hosted file

`essoar.10512189.1.docx` available at https://authorea.com/users/533807/articles/598315-anomalously-high-heat-flow-regions-beneath-the-transantarctic-mountains-and-wilkes-subglacial-basin-in-east-antarctica-inferred-from-curie-depth

Anomalously high heat flow regions beneath the Transantarctic Mountains and Wilkes Subglacial Basin in East Antarctica inferred from Curie depth

Maximilian Lowe[1,2], Ben Mather[3], Chris Green[4], Tom A. Jordan[1], Jörg Ebbing[5], Robert Larter[1]

[1] British Antarctic Survey, Cambridge, United Kingdom.

[2] The University of Edinburgh, Edinburgh, United Kingdom.

[3] The University of Sydney, Sydney, Australia.

[4] University of Leeds, Leeds, United Kingdom.

[5] Christian-Albrechts-Universität zu Kiel, Kiel, Germany.

Corresponding author: Maximilian Lowe (maxwe32@bas.ac.uk)

Key Points:

- New Curie Depth Point and geothermal heat flow maps for the Transantarctic Mountains and Wilkes Subglacial Basin in East Antarctica
- High heat flow beneath the Transantarctic Mountains reinforces the idea of thermal support of the topography of the mountain range
- Heat flow estimates agree with recent active volcanoes and topographic feature in the Wilkes Subglacial Basin

Abstract

The Transantarctic Mountains (TAM) separate the warmer lithosphere of the West Antarctic rift system and the colder East Antarctic craton. Low velocity zones beneath the TAM imaged in recent seismological studies have been interpreted as warm low-density mantle material, suggesting a strong contribution of thermal support to the uplift of the TAM. We present new Curie Depth Point (CDP) and geothermal heat flow (GHF) maps of the northern TAM and adjacent Wilkes Subglacial Basin (WSB) based on high resolution magnetic airborne measurements. We find shallow CDP and high GHF, beneath the northern TAM reinforcing the idea of thermal support of the topography of the mountain range. Additionally, locally high GHF is observed in the Central Basin of the WSB and the Rennick Graben, which has not been resolved previously, while the broader WSB show lower GHF. Across the study area the GHF values range from 30 to 110 mW/m^2. Lastly, we compare our CDP estimates to recent Moho depth estimates and our GHF estimates to sparse in situ GHF measurements as well

as to existing continent-wide GHF estimates, which shows closed agreement to previous seismic estimates.

Plain language summary

The Transantarctic Mountains are a long mountain range separating the ancient East Antarctic region from the younger West Antarctic region. Recent studies estimated the speed of acoustic waves generated from earthquakes found a region where the waves moved slowly beneath the Transantarctic Mountains. Slow wave speeds are believed to be caused by warmer rocks in the area, which provide thermal support for the mountain range.

We present heat flow maps, which describe the heat transfer from the interior of the earth to the surface. The estimated heat flow is based on "Curie depth points", which describes the depth at which magnetic rocks lose their ability to generate a magnetic field due to increasing temperature. This temperature is called the Curie temperature, which is around 580 °C for magnetite, the most common magnetic mineral in the Earth's crust. The heat flow at the surface is estimated from depth at which this temperature is reached.

We find elevated heat flow beneath the Transantarctic Mountains, which supports the idea of warmer rocks that provide thermal support for the Transantarctic Mountains. Additionally, we found high heat flow in deep topographic valleys of the adjacent Wilks Subglacial Basin and Rennick Graben.

1 Introduction

The evolution of both the Transantarctic Mountains (TAM) and Wilkes Subglacial Basin (WSB) (Figure 1) as well as their coupling are not fully resolved, despite their crucial role to potential future sea level rise [*DeConto and Pollard*, 2016; *Ferraccioli et al.*, 2009b; *Hansen et al.*, 2016; *Jordan et al.*, 2013; *Paxman et al.*, 2019].

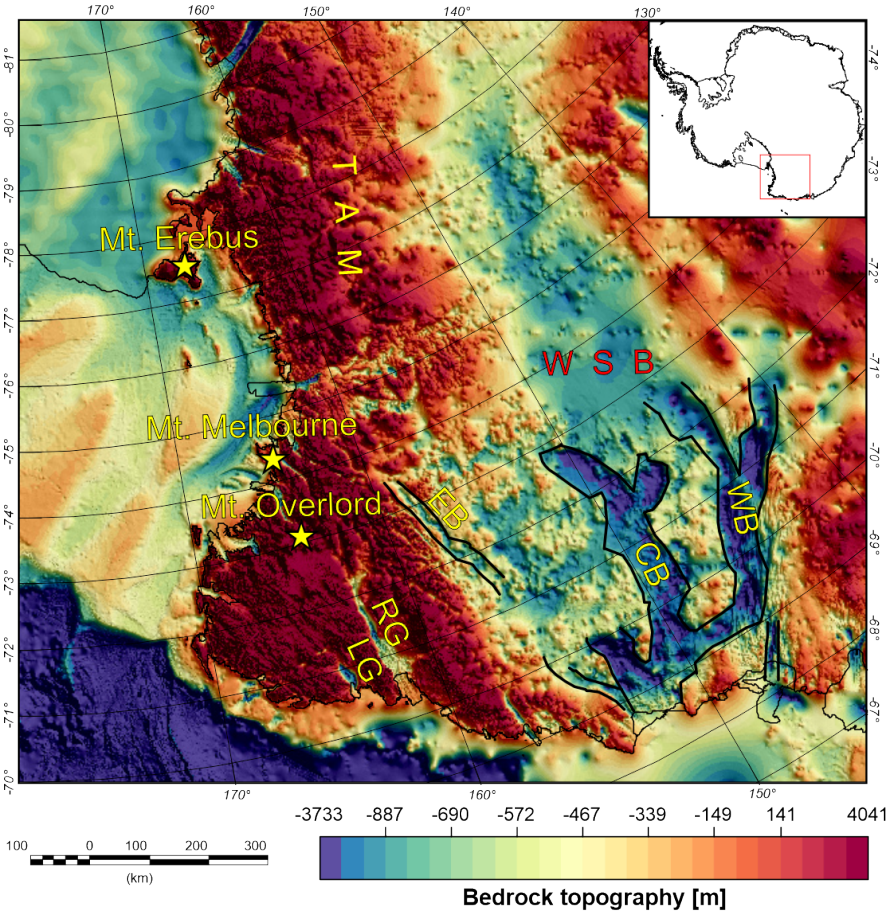

Figure 1: Bedrock topography of the Transantarctic mountains and Wilkes subglacial basin from the Bedmachine model version 2 [Morlighem et al., 2020]. Black lines delimit more deeply incised sub-basins within the wider Wilkes Subglacial Basin region. Yellow stars indicate the location of recently active volcanoes. LG, Lillie Graben; RG, Rennick Graben; EB, Eastern Basin, CB, Central Basin; WB, Western Basin; WBS, Wilkes Subglacial Basin; TAM, Transantarctic Mountains.

The Transantarctic Mountains (TAM) are the largest non-contractional mountain range on Earth (Figure 1), which divide East Antarctica from the West Antarctic Rift System [*Morelli and Danesi*, 2004; *Robinson and Splettstoesser*, 1986; *ten Brink and Stern*, 1992]. The approximately 4000 km long and up to 400 km wide mountain range, with a peak elevation of 4000 m [*Morlighem et al.*, 2020], has a complex tectonic history with numerous proposed uplift mechanisms. Uplift models include flexural uplift [*Paxman et al.*, 2019; *ten Brink et al.*, 1997; *Wannamaker et al.*, 2017; *Yamasaki et al.*, 2008], thermal mantle support [*Brenn et al.*, 2017; *Lawrence et al.*, 2006; *Smith and Drewry*, 1984]

as well as density variation and crustal thickening [*Bialas et al.*, 2007; *Huerta*, 2007]. A local study investigating crustal structures beneath the northern TAM based on receiver function data concluded that the crust beneath the TAM is up to ~46 km thick, which is significant less than the required 57 km to support the mountains isostatically [*Hansen et al.*, 2016]. They instead suggest broad flexure of the East Antarctic lithosphere and uplift along the western edge as a result of lateral heat conduction from the hotter West Antarctic mantle in line with the uplift model by [*Stern and ten Brink*, 1989; *ten Brink et al.*, 1997; *ten Brink and Stern*, 1992]. Recent studies based on new seismic tomography models [*Brenn et al.*, 2017; *Graw et al.*, 2016; *Lloyd et al.*, 2020; *Shen et al.*, 2018; *Wiens et al.*, 2021] show large low velocity zones beneath the northern TAM, which are interpreted as warm and less dense mantle material. This observation suggests that the warmer mantle beneath the highest topographic features in Northern Victoria Land, provides a strong contribution of thermal support to the uplift of this region [*Wiens et al.*, 2021].

The Wilkes Subglacial Basin (WSB) located in the hinterland of the TAM, is a major below sea level topographic feature, buried 2-3 km beneath the East Antarctic Ice Sheet (EAIS) (Figure 1). The WSB was first described from radar data in the 1970s [*Drewry*, 1976] and stretches approximately 1600 km from the George V Coast towards South Pole. The WSB comprises one of the largest marine-based sectors of the EAIS [*Ferraccioli et al.*, 2009a; *Ferraccioli et al.*, 2009b]. The bedrock elevation reaches depths of more than 2000 m below sea level within the locally more deeply incised sub-basins [*Ferraccioli et al.*, 2009a; *Morlighem et al.*, 2020]. The WSB is about 600 km wide close to the George V coast [*Ferraccioli et al.*, 2009b], decreasing to <100 km towards South Pole [*Studinger et al.*, 2004]. The modern landscape formation of the WSB is interpreted as being associated with flexural process of the TAM uplift and glacial erosion [*Ferraccioli et al.*, 2009a; *Jordan et al.*, 2013; *Paxman et al.*, 2018; *Paxman et al.*, 2019]. The WSB is bounded by the Terre Adélie Craton, West of the Mertz shear zone [*Finn et al.*, 2006] and by the TAM on the East.

Submarine basins like the WSB pose a potentially high, but poorly constrained risk for future sea level rise, as they are more vulnerable to melting by warming of the surrounding ocean. Such melting could potentially trigger mechanisms of unstable retreat [*Pollard et al.*, 2015; *Schoof*, 2007]. Significant long-term contribution is predicted from the WSB region to future sea-level rise over the next two centuries and eventual retreat of the ice sheet into the northern WSB by the year 2500 [*DeConto and Pollard*, 2016; *Stokes et al.*, 2022]. Geothermal heat flow (GHF) is identified as a crucial contribution from the solid Earth which interacts with the cryosphere [*Davies*, 2013; *Fahnestock et al.*, 2001]. GHF influences the rheology of the ice and can lead to basal melting, factors which can both facilitate enhanced ice flow and consequently influence ice sheet stability [*Larour et al.*, 2012; *Llubes et al.*, 2006; *Pittard et al.*, 2016; *Winsborrow et al.*, 2010]. GHF is therefore a crucial parameter for modelling ice sheets and future sea-level rise [*Matsuoka et al.*, 2012; *Pattyn*, 2010; *Pattyn et al.*, 2016; *Pittard et al.*, 2016; *Van Liefferinge et al.*, 2018; *Whitehouse et al.*, 2019; *Winkelmann*

et al., 2011]. GHF also has the potential to shed light on the region's long-term tectonic evolution. Areas of elevated heat flow are often associated with regions of shallow warm mantle, and provide a test for the hypothesis that incursion of warmer West Antarctic mantle beneath the TAM provides thermal support to the mountain range, as suggested by [*Hansen et al.*, 2016; *Smith and Drewry*, 1984]

Although in-situ GHF measurements would be very significant, they are almost non-existent [*Burton-Johnson et al.*, 2020]. Consequently, GHF models are inferred from different geophysical techniques. Those techniques can be subdivided into two broad categories: modelling of geophysical data and machine learning or statistical correlation. Modelling approaches include determining the depth of the 580 °C isotherm from magnetic data and subsequently calculating GHF from this isotherm [*Martos et al.*, 2017] as well as calculating GHF based on seismologically derived upper mantle temperature [*An et al.*, 2015]. Statistical models include correlating seismic velocity structures in Antarctica to those in areas with good constraints on GHF [*Shen et al.*, 2020], machine learning techniques where the model is trained in areas where the GHF is well understood [*Lösing and Ebbing*, 2021; *Lösing et al.*, 2020] and statistical similarity of multiple datasets which are compared to global GHF catalogues [*Stål et al.*, 2021]. The large-scale distinction between East and West Antarctica is recognised in most GHF models [*An et al.*, 2015; *Lösing and Ebbing*, 2021; *Martos et al.*, 2017; *Shen et al.*, 2020; *Stål et al.*, 2021]. However, existing continental scale GHF models for Antarctica show remarkable inconsistency on a more local scale (Figure 2).

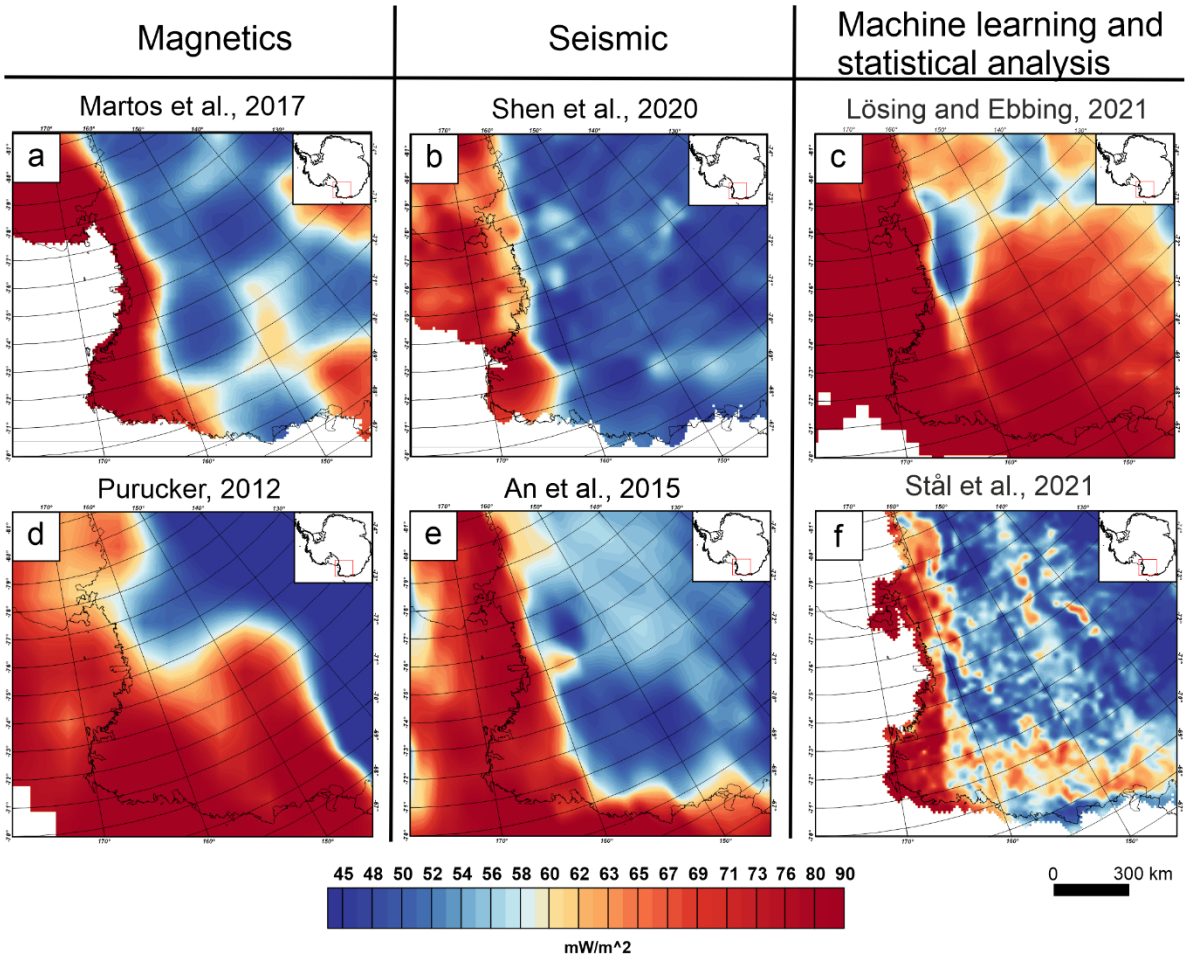

Figure 2: Continent-wide geothermal heat flow models derived from various geophysical approaches. a) magnetic derived GHF model [Martos et al., 2017]. b) seismological derived GHF model [Shen et al., 2020]. c) GHF model derived from multiple data sets via Machine Learning [Lösing and Ebbing, 2021]. d) GHF map derived from satellite magnetic data [Purucker, 2012 an update of Fox Maule et al., 2005] e) Seismologically inferred GHF model [An et al., 2015]. f) GHF estimates derived by statistical analyses of multiple data sets [Stål et al., 2021].

In this study high resolution airborne magnetic data and spectral analysis are used to improve existing GHF models in the TAM and WSB area. We test if elevated geothermal heat flow is imaged beneath the northern most part of the TAM to verify independent seismological findings of proposed thermal support for uplift in northern Victoria Land [*Hansen et al.*, 2016; *Lloyd et al.*, 2020; *Wiens et al.*, 2021]. In addition, our study reveals spatial variation of GHF in the WSB which previous models were not able to image.

2 Data

The ADMAP-2 compilation includes 3.5 million line-km of aeromagnetic and marine magnetic data in Antarctica and the Southern Ocean south of 60 °S [*Golynsky et al.*, 2018]. The gridded ADMAP-2 product (Figure 3a) has a grid spacing of 1.5 km and its production included correction for the International Geomagnetic Reference Field, diurnal effects correction, high-frequency error correction, levelling, regional gridding, and merging of regional grids into a continent-wide compilation [*Golynsky et al.*, 2018].

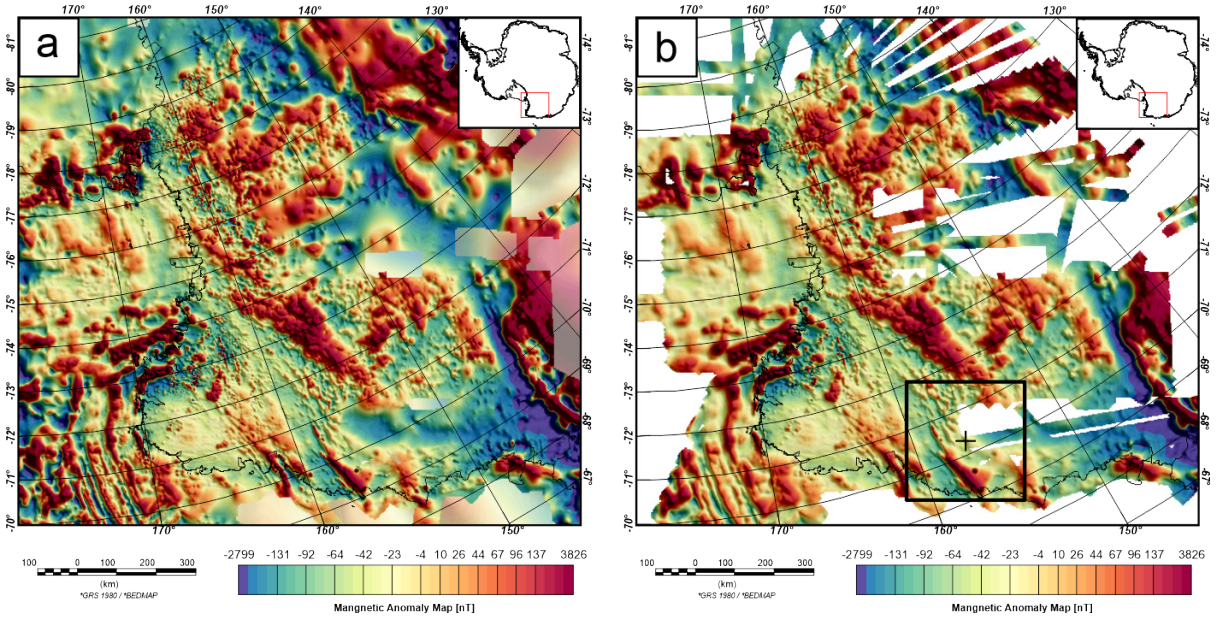

Figure 3: a) ADMAP-2 with a grid spacing of 1.5 km [Golynsky et al., 2018] superimposed on Satellite Magnetic Anomaly Map from the LCS 1 model [Olsen et al., 2017]. b) Selected recent ADMAP-2 magnetic data, which was re-gridded and upward continued to a constant height of 4 km. Black cross and black rectangle indicate the centroid and extension of window 645 with a window size of 300 km.

For this study only recent (~2000 - present) aeromagnetic data was selected from ADMAP-2 and a blanking distance of 15 km from flight lines was applied (Figure 3b). This was done for two reasons: a) To ensure that only flight lines with high precision positioning tracing (GPS) are used and b) interpolation between widely-spaced flight line spacing is removed. Data was re-interpolated onto a 1.5 by 1.5 km mesh using a minimum curvature technique. The resulting magnetic grid was then upward continued to a constant height of 4 km above the ellipsoid (Figure 3b), based on the flight elevation data available in the ADMAP-2 compilation (See supplementary section S1).

3 Method

Magnetic materials typically lose their susceptibility (ability to generate a strong magnetic field) with increasing temperature [*Langel and Hinze*, 1998]. For magnetite, thought to be the most significant magnetic mineral in the crust, this so-called Curie temperature is ~580 °C [*Telford et al.*, 1990]. The depth at which the crust reaches this temperature, and most rocks lose their magnetic properties, is the Curie Depth Point (CDP) and defines the Curie isotherm within the crust [*Haggerty*, 1978; *Núñez Demarco et al.*, 2020]. Estimating the depth of magnetic sources using the power spectrum of magnetic data was first established as a method in 1970 [*Spector and Grant*, 1970]. Since then, numerous methods were developed to estimate the bottom of all magnetic sources in an area, and hence the CDP. Established methods to estimate the CDP include the centroid method [*Bhattacharyya and Leu*, 1975a; b; *Blakely*, 1996; *Okubo et al.*, 1985; *Tanaka et al.*, 1999; *Treitel et al.*, 1971] spectral peak method [*Blakely*, 1996; *Connard et al.*, 1983] and fractal methods [*A.R. Bansal and Dimri*, 2005; *A. R. Bansal et al.*, 2011; *Bouligand et al.*, 2009; *Kumar et al.*, 2021; *Li et al.*, 2019; *Mather and Fullea*, 2019; *Maus and Dimri*, 1995; *Maus et al.*, 1997; *Salem et al.*, 2014; *Todoeschuck et al.*, 1992] for a more detailed discussion of those methods the reader is referred to [*Núñez Demarco et al.*, 2020; *Ravat et al.*, 2007].

In our study the centroid method after [*Tanaka et al.*, 1999] is used to calculate the CDP. This approach assumes a random distribution of magnetic sources in the crust. The radially averaged power spectrum was calculated using the python library Pycurious [*Mather and Delhaye*, 2019].

The radially averaged power spectrum $\Phi\Delta(\ )$ is defined as:

$$\Phi_{\Delta \mathrm{T}}(|k|) = Ae^{-2|k|Z_t}\left(1 - e^{-|k|(Z_b - Z_t)}\right)^2 \tag{1}$$

Where A is a constant, is the spatial wavenumber defined as $=2\ /\ ,$ where is the wavelength), is the top of assumed magnetic source and is bottom of assumed magnetic source and therefore $-$ describes the thickness of the magnetic source [*Mather and Delhaye*, 2019; *Tanaka et al.*, 1999].

For shorter wavelengths (generally less than twice the source thickness), this approximates to:

$$ln[\Phi_{\Delta \mathrm{T}}(|k|)^{\frac{1}{2}}] = \ln B - |k|Z_t \tag{2}$$

Where B is constant [*Mather and Delhaye*, 2019; *Tanaka et al.*, 1999].

Equation (1) can be rewritten, with Z_0 as the centroid depth of the magnetic source [*Mather and Delhaye*, 2019; *Tanaka et al.*, 1999].

$$\Phi_{\Delta \mathrm{T}}\left(|k|\right)^{\frac{1}{2}} = Ce^{-|k|Z_0}\left(e^{-|k|(Z_t - Z_0)} - e^{-|k|(Z_b - Z_0)}\right) \tag{3}$$

Where C is a constant.

For long wavelengths, where 2 is the magnetic source thickness we obtain equation 4 and 5 [*Mather and Delhaye*, 2019; *Tanaka et al.*, 1999].

$$\Phi_{\Delta \mathrm{T}}\left(|k|\right)^{\frac{1}{2}} = Ce^{-|k|Z_0}\left(e^{-|k|(-d)} - e^{-|k|(d)}\right) \approx Ce^{-|k|Z_0} 2|k|\mathrm{d} \tag{4}$$

$$\ln\left\{\frac{\Phi_{\Delta \mathrm{T}}\left(|k|\right)^{\frac{1}{2}}}{|k|}\right\} = \ln D - |k|Z_0 \tag{5}$$

The depth to the top ( ) and centroid ( ) of the magnetic source are recovered by fitting a linear regression through the high-wavenumber and low-wavenumber part of the radially averaged spectrum of $ln[\Phi_{\Delta \mathrm{T}}\left(|k|\right)^{\frac{1}{2}}]$ and $\ln\left\{\frac{\Phi_{\Delta \mathrm{T}}(|k|)^{\frac{1}{2}}}{|k|}\right\}$ in equation 2 and 5 respectively (Tanaka et al., 1999). With Z_t and $\mathrm{Z_0}$ the base of the magnetic source (Z_b) can be estimated applying equation 6 [*Mather and Delhaye*, 2019; *Tanaka et al.*, 1999].

$$Z_b = Z_0 - (Z_t - Z_0) = 2Z_0 - Z_t \tag{6}$$

3.1. Data preparation and window size

The window size is an influential parameter in spectral methods because it ultimately determines the maximum wavelength which will be captured in the subgrid and therefore controls the maximum depth that can be recovered [*Núñez Demarco et al.*, 2020].

Various authors make conflicting suggestions regarding appropriate window sizes [*Núñez Demarco et al.*, 2020] ranging from 3 times the depth of the magnetic layer [*Hussein et al.*, 2013] to 10 times the recovered depth of the magnetic layer [*Ravat et al.*, 2007]. In contrast [*Li et al.*, 2017] use several window sizes, where the recovered depths are averaged into the final CDP grid. [*Bouligand et al.*, 2009] use an iterative approach, where they expand the window around a given grid point until a depth of the bottom of the magnetic layer $\mathrm{Z_b}$ smaller than a tenth of the window size is recovered. In this study, we test recovery of the CDP beneath the TAM and WSB using analysis window sizes of 200 km by 200 km, 300 km by 300 km and 400 km by 400 km following the recommendation for a window size of 5 to 10 times the recovered CDP [*Ravat et al.*, 2007]. We discuss the differences in absolute value, resolution and accuracy of recovered CDP, and justify our choice of a 300 km preferred window size later (section 5).

The Fourier transformation requires the windowed data to have no data gaps. However, Antarctica is not fully covered by magnetic airborne surveys. Previous studies in Antarctica have bypassed this problem by merging the airborne data with satellite magnetic data[*Dziadek et al.*, 2021; *Martos et al.*, 2017]. Satellite magnetic data for estimating CDP should be used with caution because the analytical window functions as a high pass filter removing all wavelengths longer than the window size. However, satellite derived magnetic models only contain longer wavelengths, similar in length to the typical analysis window, for example the satellite derived magnetic model MF7 [*Maus et al.*, 2007] contains only wavelength larger than 300 km. It is therefore questionable whether merged satellite and airborne magnetic data can provide a representative CDP estimation due to the limited wavelengths in the power spectrum. This issue was recently discussed by *Pappa and Ebbing,* [2021]. In our study the problem regarding data gaps within the airborne data is overcome by interpolation of the airborne data to ensure only direct observations contribute to the spectral content in the window. Subsequently, we estimate the data coverage of every window and discard windows with less than 80% data coverage to ensure that the recovered CDP estimates are not dominated by interpolation effects.

It is common for spectral methods that the study area is subdivided into windows which have a large overlap between them [*Audet and Gosselin*, 2019; *Blakely*, 1988; *Bouligand et al.*, 2009; *Idárraga-García and Vargas*, 2018; *Leseane et al.*, 2015; *Okubo et al.*, 1985]. The overlap increases the number of depth estimates and is expected to increase resolution up to a point, which allows the investigation of lateral variations in Curie point depths through the study area. it also allows smoothing of the more closely spaced CTD values (see supplementary information section s2). In this study we use a step size of 20 km between the analytic window, which results in a large overlap between the windows. A Hanning taper is applied to the windowed subgrid in the space domain to remove edge discrepancies. No further modification, corrections or filters have been applied to the magnetic grid and power spectrum in line with recommendations from previous authors [*Audet and Gosselin*, 2019; *Núñez Demarco et al.*, 2020; *Ravat et al.*, 2007].

Applying this approach, with a threshold of 80% data coverage, we obtain 2161 valid windows for a window size of 200 km, 1933 windows for a window size of 300 km and 1685 windows for the window size of 400 km. Our approach is limited to regions with relatively good airborne data coverage and therefore cannot be applied to the entire Antarctic continent.

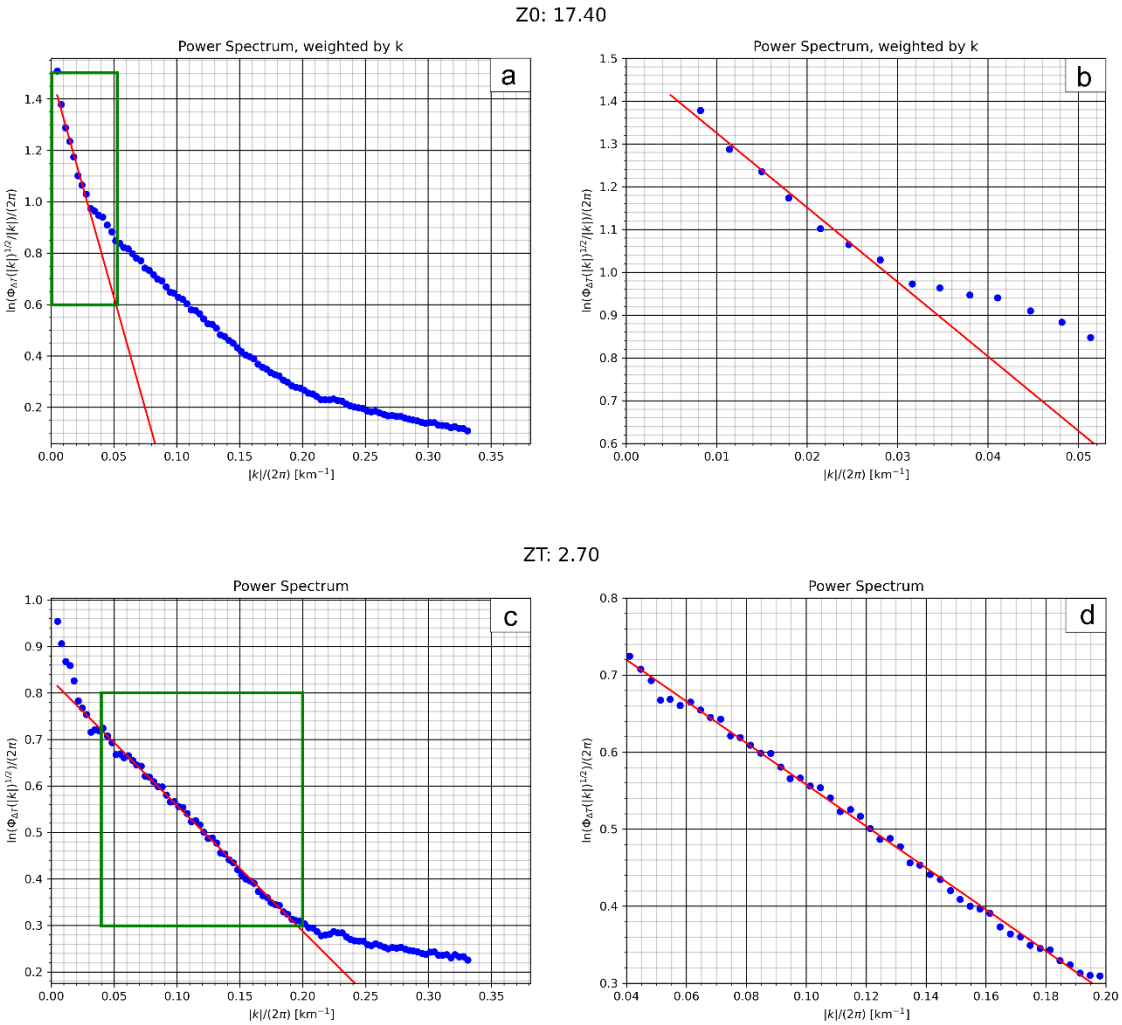

Figure 4: Power spectrum from window 645, centroid location and extension of the window is given in Figure 3b. a) Power spectrum weighted by k to estimate Z_0. Red line represents the fitted line through the low wavenumber part of the power spectrum. Green rectangle illustrates zoom in range for b). b) zoomed in power spectrum weighted by k. c) Power spectrum to estimate Z_t. Red line represents the fitted line through the high wavenumber part of the power spectrum. Green rectangle illustrates zoom in range for d). d) zoomed in power spectrum.

A fixed wavenumber range is used to estimate the CDP in each window. Z_0 is calculated in the wavenumber range 0.006 - 0.033 $k/2$ (167-30 km wavelength) and Z_t is calculated in range 0.04 - 0.2 $k/2$ (25-5 km wavelength) respectively.

The ideal wavenumber range for Z_0 is defined as the first linear segment after the spectral peak in the low wavenumber part of the power spectrum, while the ideal range for Z_t is defined as the second linear segment in the power spectrum. The linear regression (Figure 4) to estimate Z_t and Z_0 is carried out using the function *curve fit* from the python library SciPy learn [*Virtanen et al.*, 2020]. The uncertainty of the fitted slope is calculated by estimating the standard deviations from the covariance matrix by taking the square root of the diagonals (equation 6) and propagating the uncertainty (equation. 7).

$$\sigma_{\text{slope}} = \sqrt{\text{Cov}_{\text{diag}}} \tag{6}$$

$$\sigma_{\text{CDP}} = \sqrt{\sigma^2_{slope[Z_t]} + 2(\sigma^2_{\text{slope}[Z_0]})} \tag{7}$$

We note that the estimated uncertainty is a formal error, which describes how well the linear regression fits the radially averaged power for the predefined wavenumber range. The absolute uncertainty of the CDP estimation may surpass this formal error (see section 5.2).

CDP estimations, which are an approximation for the 580 °C Curie isotherm can be used as a proxy for geothermal heat flow. Where CDPs are shallow a higher geothermal heat flow is expected and vice versa. A first order approximation of GHF from CDP estimates can be inferred from Fourier's Law (equation 8) [*Núñez Demarco et al.*, 2020; *Turcotte and Schubert*, 2002].

$$Q = -K\frac{\partial T}{\partial z} = -K\,\frac{T_c - T_{\text{surface}}}{Z_b} \tag{8}$$

Where Q is the heat flux at the bedrock interface, T_c is the Curie temperature (580 °C), $T_{Surface}$ is the surface temperature, Z_b is the Curie depth point and K is the thermal conductivity. Here, a thermal conductivity of 2.5 W/mK is used, which is the average thermal conductivity of igneous rocks [*Clauser and Huenges*, 1995; *Goes et al.*, 2020; *Hasterok et al.*, 2018; *Jennings et al.*, 2019]. Temperature at the bedrock surface ($T_{surface}$) is set to 0 °C in line with previous spectral analysis studies in Antarctica [*Dziadek et al.*, 2021; *Martos et al.*, 2017]. Assuming 0 °C at the bedrock interface is sufficient since most of the bottom of the ice sheet has been calculated to be at the pressure melting point around -2 °C with a variation of a few °C, which results in a "wet base" of the icesheet [*Pattyn*, 2010]. This assumption breaks for areas with dry base ice sheet and areas with no ice cover. Over most of this region annual mean surface temperatures are -20 to -50 °C [*Wang and Hou*, 2009]. We performed a sensitivity test for the dry base ice sheet and ice-free scenario assuming an annual surface temperature of -30 °C (Figure S3). The GHF increases by a maximum of 6 mW/m^2 and by a mean value of 4 mW/m^2, which is below the error estimation and therefore is a negligible effect; using an ice surface temperature is also problematic due to the potential for melting/freezing in the ice as well as fluid flow. Equation 8 is a strong simplification of the real world

since it neglects spatial variation of thermal conductivity caused by e.g., geology as well as any heat production in the area due to e.g., radiative heat production in crustal rocks. Those parameters are strongly influenced by the composition of the present crustal rocks, which are poorly constrained in Antarctica due to the thick overlaying ice sheet [*Burton-Johnson et al.*, 2020]. [*Martos et al.*, 2017] accounted for crustal heat production by using a constant value for the entire Antarctic continent, which does not help the conversation on spatial GHF variation caused by heterogeneity within the crust.

4 Results

The CDP estimates range between 15 and 35 km (Figure 5 a-c). A low CDP value indicates a shallow Curie isotherm of 580 °C and therefore implies a higher heat flow and vice versa. A prominent shallow CDP province is present beneath the TAM between -78° and -72 ° latitude for all three window size configurations. In the area of the Rennick Graben a linear shallow feature is visible in the 200 and 300 km windows (Figure 5 a-b) but is much subdued in the 400 km window (Figure 5 c). Another linear feature is observed in the Central Basin (Figure 5 a-b).

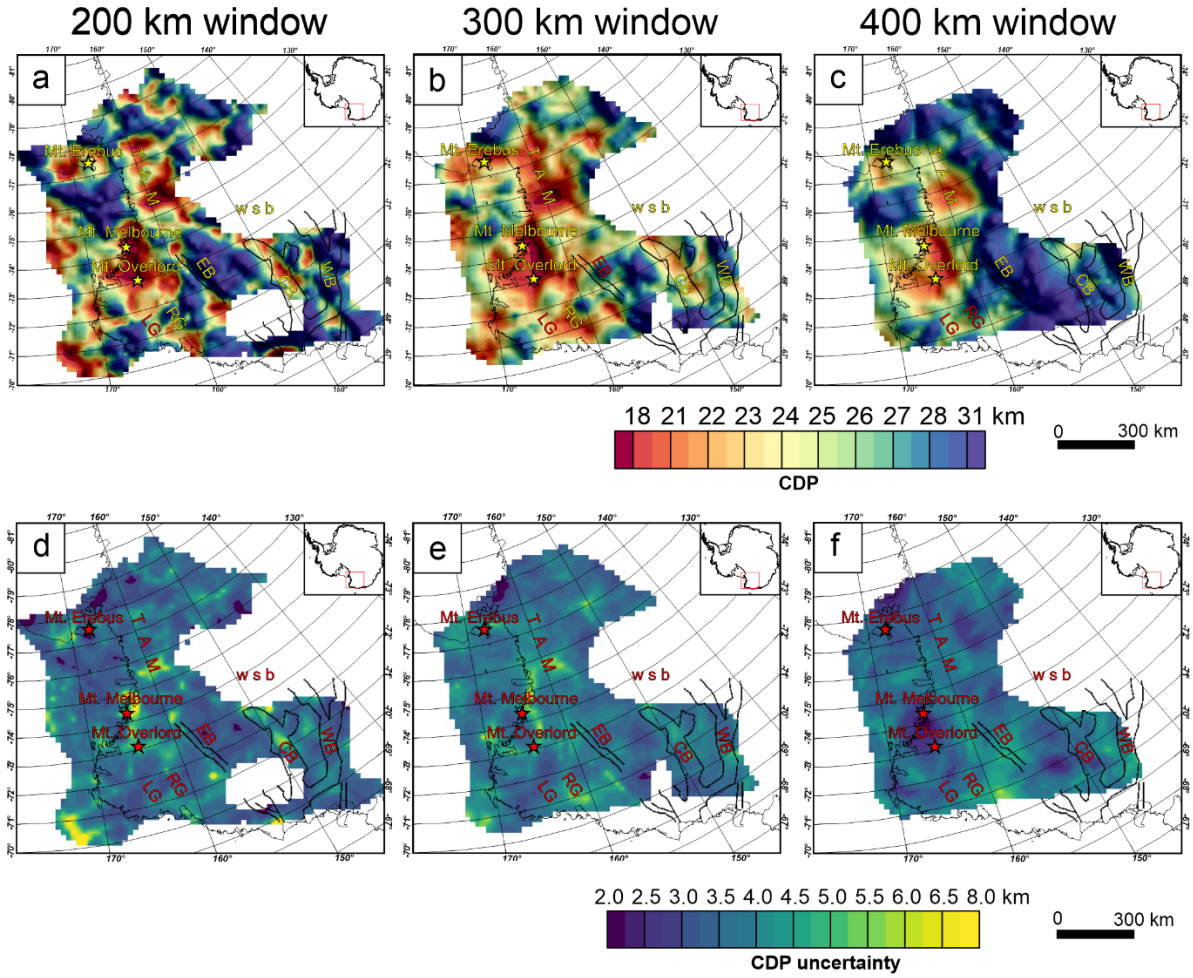

Figure 5: Upper row gives CDP estimates for different window sizes. Lower row illustrates the corresponding uncertainty. a) CDP based on a 200 by 200 km window. b) CDP estimates obtained with a 300 by 300 km window. c) Calculated CDP with a 400 by 400 km window. d) uncertainty for CDP estimates based on a 200 by 200 km window. e) uncertainty for CDP estimates obtained with a 300 by 300km window. f) uncertainty for CDP estimates with a window size of 400 by 400km. LG, Lillie Graben; RG, Rennick Graben; EB, Eastern Basin, CB, Central Basin; WB, Western Basin; WSB, Wilkes Subglacial Basin; TAM, Transantarctic Mountains.

Again, this feature is subdued in the 400 km window (Figure 5c). West of the Central Basin, deeper CDP values are observed, indicating an overall colder thermal structure. CDP estimates from the 200 km window have a higher frequency in their spatial pattern compared to window size configurations of 300 km and 400 km (Figure 5a-c). With increasing window size, the range of

recovered CDP decreases, while the mean depths become deeper (Figure 5a-c, Figure 7 a-c). Moreover, the estimated uncertainties decrease with increasing window size (Figure 5 a-f). Linear transformation of CDP to GHF maps (see equation. 8) yielded estimates ranging from 38 to 110 mW/m^2. The spatial patterns in the GHF maps (Figure 6 a-c) are identical to those observed in the CDP map (Figure 6a-c) due to the linear relationship between both maps. Again, the range of GHF values decreases with increasing window size while the error decreases also with increasing window size (Figure 6 a-f).

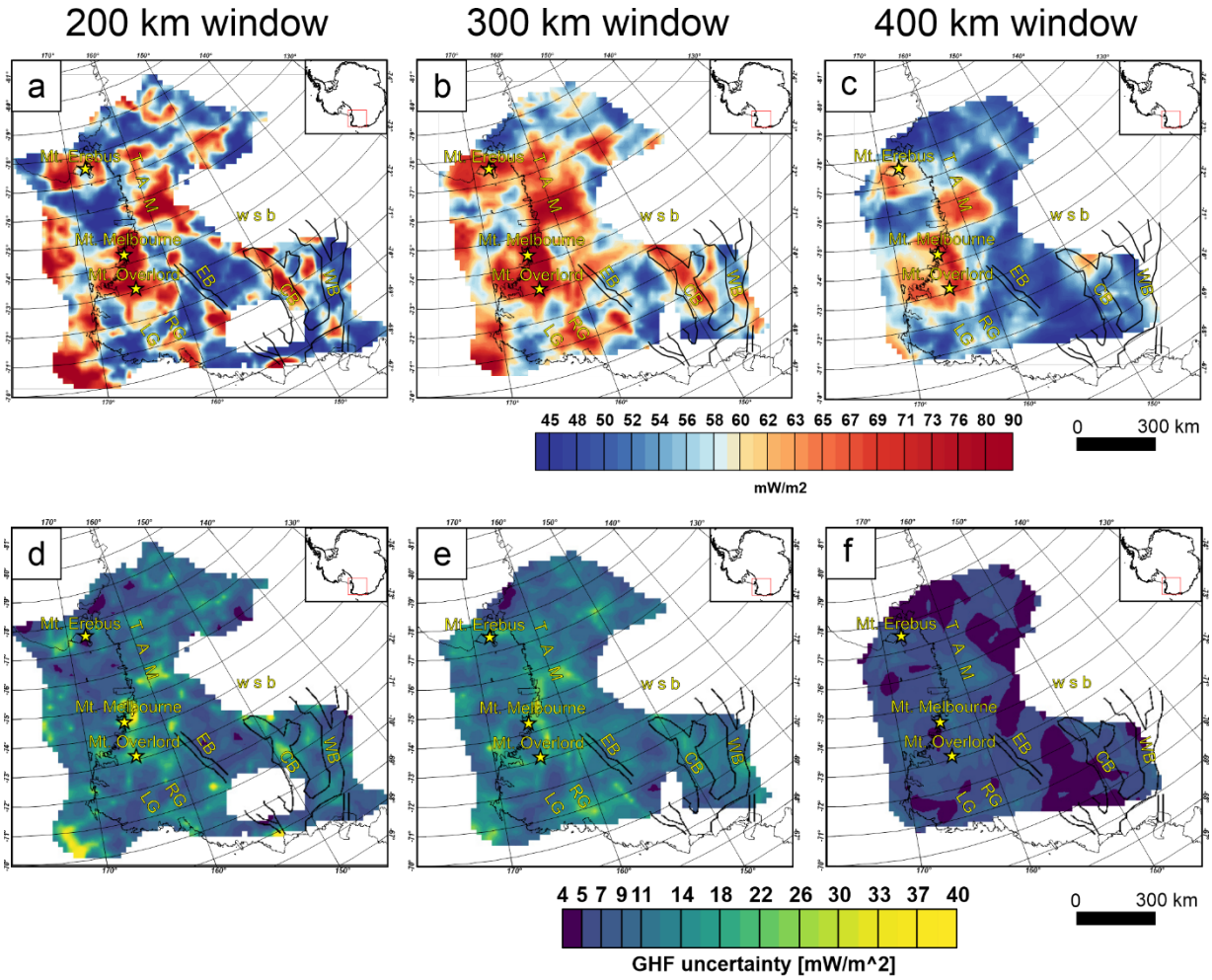

Figure 6: Upper row gives GHF estimates for different window sizes. Lower row illustrates the corresponding uncertainty. a) GHF based on a 200 by 200 km window. b) GHF estimates obtained with a 300 by 300 km window. c) Calculated GHF with a 400 by 400 km window. d) uncertainty for GHF estimates based on a 200 by 200 km window. e) uncertainty for GHF estimates obtained with a

300 by 300km window. f) uncertainty based on GHF estimates with a window size of 400 by 400km. LG, Lillie Graben; RG, Rennick Graben; EB, Eastern Basin, CB, Central Basin; WB, Western Basin; WSB, Wilkes Subglacial Basin; TAM, Transantarctic Mountains.

5 Discussion

Results recovered from a window size of 300 km and 400 km are preferred for multiple reasons: First, the recommendation for an optimal window size is 5 – 10 times the recovered CDP [*Ravat et al.*, 2007] (see section 3.1). The largest portion of recovered CDP across all window sizes is between 25 and 30 km (Figure 7). Aiming for a window size which is 10 times the recovered CDP the preferred windows size must be larger than 250 km and thus the 300 km window size in our study is best suited to satisfy this recommendation. In addition, a window size of 300 km recovers a larger number of valid CDP estimates for the study area in comparison to the 400 km window size (Figure 7 a-c).

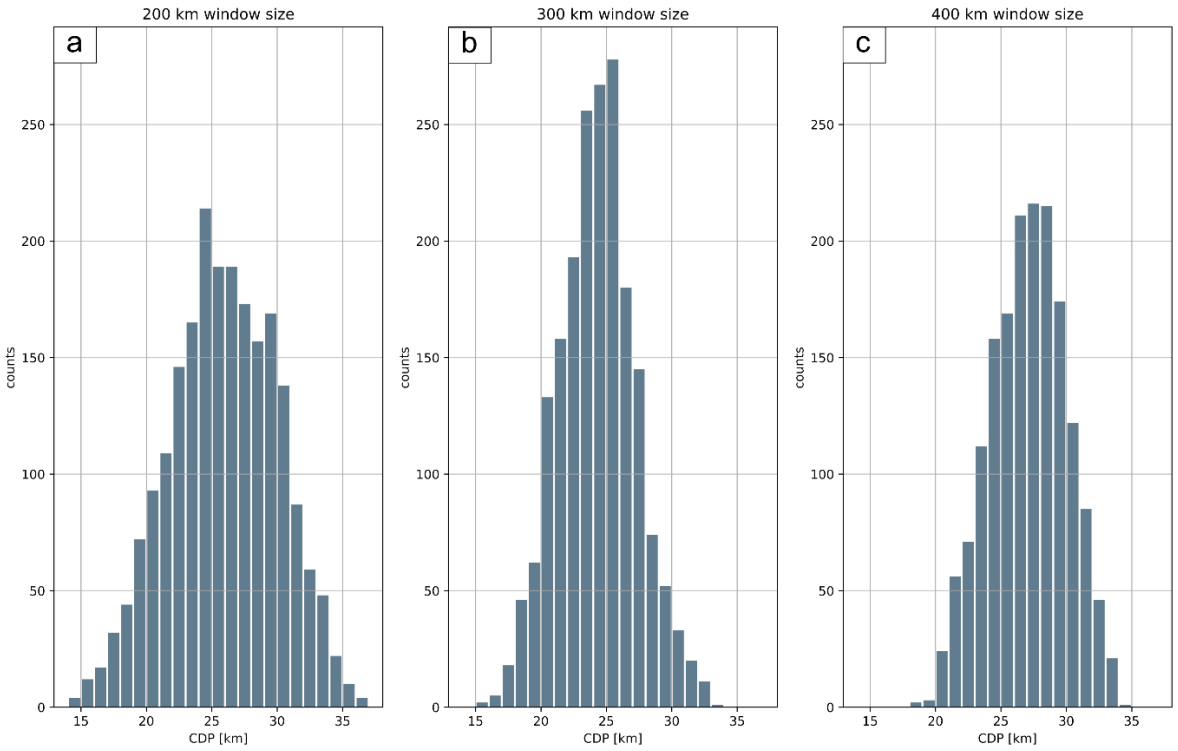

Figure 7: Histogram of recovered CDP depth for different window sizes with a bin size of 1km. a) CDP estimates recovered from 200 by 200 km windows. b) CDP estimates obtained using 300 by 300 km windows. c) Recovered CDP based on 400 by 400 km windows.

The estimated error for the CDP estimates based on the fitting of the radially averaged power spectrum decreases with increasing window size (Figure 5 d-f), which points in the direction of missing low wavenumber content in the 200 km window, while larger window sizes are stabilised due to capturing a wider bandwidth. Moreover, high frequency of spatial variation in the CDP is observed in the 200 km window (Figure 5 a), while CDP from a larger window size (Figure 5 b-c) shows less spatial variation. A large change between the results obtained from a 200 to 300 km window is observed, although many key features persist. A much smaller change is observed between the result obtained from a 300 and 400 km window, suggesting the recovered CDP values stabilise for windows larger than 200 km. Lastly, CDP resulting from a 300 km window recovered spatial patterns, which are consistent with geological and topographic features like the Rennick Graben and the Central Basin. Based on the arguments above we prefer results obtained from a window size of 300 km.

CDP estimates are the result of the average Curie depth within the analysing window, although a strong depth variation within the window may bias the estimation to deeper or shallower values. Moho depth maps are a good control mechanism since Curie depths deeper than the Moho interface would imply that the upper mantle is magnetic (although this possibility has been suggested [*Ferré et al.*, 2014]). CDP estimations of this study are above the Moho interface onshore with a few exceptions near the edge of the magnetic data coverage (Figure 8). CDP estimate offshore in the Ross Sea show isolated areas with deeper CDP estimates compared to the Moho map from *Pappa et al.,* [2019].

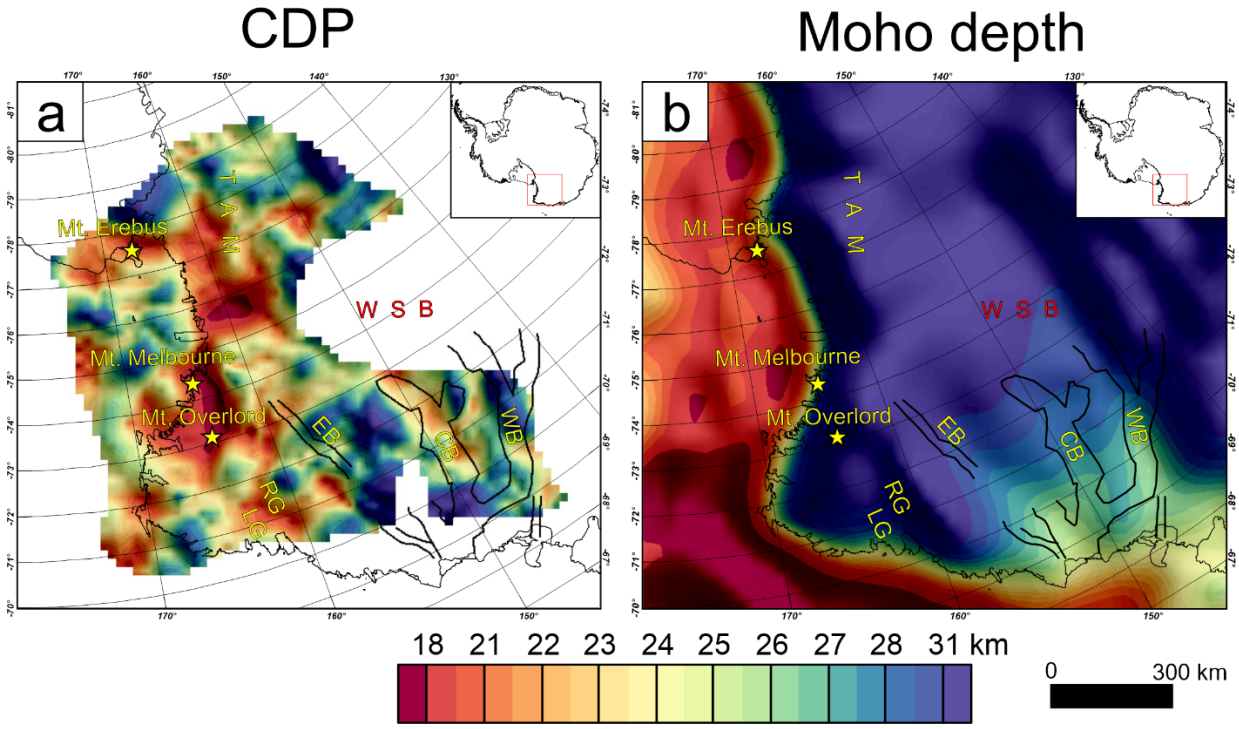

Figure 8: a) CDP estimates recovered with a 300 km window size. b) Moho depth map inferred from satellite gravity inversion [Pappa et al., 2019]. Yellow stars indicate the location of recent active volcanoes. LG, Lillie Graben; RG, Rennick Graben; EB, Eastern Basin, CB, Central Basin; WB, Western Basin; WSB, Wilkes Subglacial Basin; TAM, Transantarctic Mountains.

5.1 Uncertainty of CDP and GHF estimation

Uncertainty arising from fitting the slope of the predefined wavenumber range varies between 2 and 8 km throughout the study area (Figure 5 d-f), which translate to an uncertainty of 2.9 mW/m^2 to 48.8 mW/m^2 for the GHF estimation. Uncertainty associated with choosing inappropriate size and range of the wavenumbers to calculate Z_0 *and* Z_t can lead to significantly different CDP results of the order of multiple km (See supplementary information section S4). Uncertainty from the chosen window size is in the order of a few km (Figure 5, Figure 7). With increasing window size, the average recovered depths increase, while fewer extreme CDP values are recovered (Figure 5, Figure 7). Moreover, the composition of the magnetic material itself induces uncertainty since the Curie temperature is not a universal 580 °C for all minerals [*Blakely*, 1988; *Haggerty*, 1978; *Núñez Demarco et al.*, 2020]. However, the effect of the mineral composition is almost impossible to quantify. Lastly, the linear transformation of CDP to GHF (eq. 8) does not consider heat production within the crust and assumes a constant thermal conductivity, which is a strong simplification of the

crustal properties.

It is important to consider these effects when using absolute values of GHF estimates derived from bottom of the magnetic layer methods. However, many of the uncertainties discussed above relate to the absolute value of the CDP across the study. This method provides a robust tool to imaging relative variation in CDP.

5.2 comparison to in-situ GHF measurements and previous GHF models

The global GHF catalogue [*Lucazeau*, 2019] reports a few in situ measurements for the study area (Figure 9). These measurements use different techniques and equipment. Measurements in our study area have been conducted from boreholes, sediment and ice probes [*Lucazeau*, 2019]. The measurements in the database are rated from A to C based on the variation of heat with depths and Z for not specified. A rated GHF measurements (circles in Figure 9) are very sparse in the area. The three southernmost (longitude from 163° to 165°, latitude from -77° to -77.7°) A rated measurements are conducted in boreholes and consistent with our GHF estimates. A rated measurements offshore are aligned at the edge of a high heat flow pattern. However, the negative heat flow pattern offshore arises from CDP estimates, which are below the Moho interface and therefore are less trustworthy as discussed in section 5. B and Z rated GHF measurements are overall consistent with our GHF estimates. C rated measurements onshore (triangles Figure 9) are in strong disagreement with our findings. Previous GHF models based on machine learning and multi statistical similarity analysis [*Lösing and Ebbing*, 2021; *Stål et al.*, 2021] use in situ measurements in their approach. However, [*Stål et al.*, 2021] only used A rated GHF measurements, while [*Lösing and Ebbing*, 2021] did not discriminate the measurements. We categorise the three borehole measurements taken beneath the McMurdo ice Shelf (longitude from 163° to 165°, latitude from -77° to -77.7°) to be the most trustworthy and are more cautious in regard to measurements obtained using sediment and ice probes.

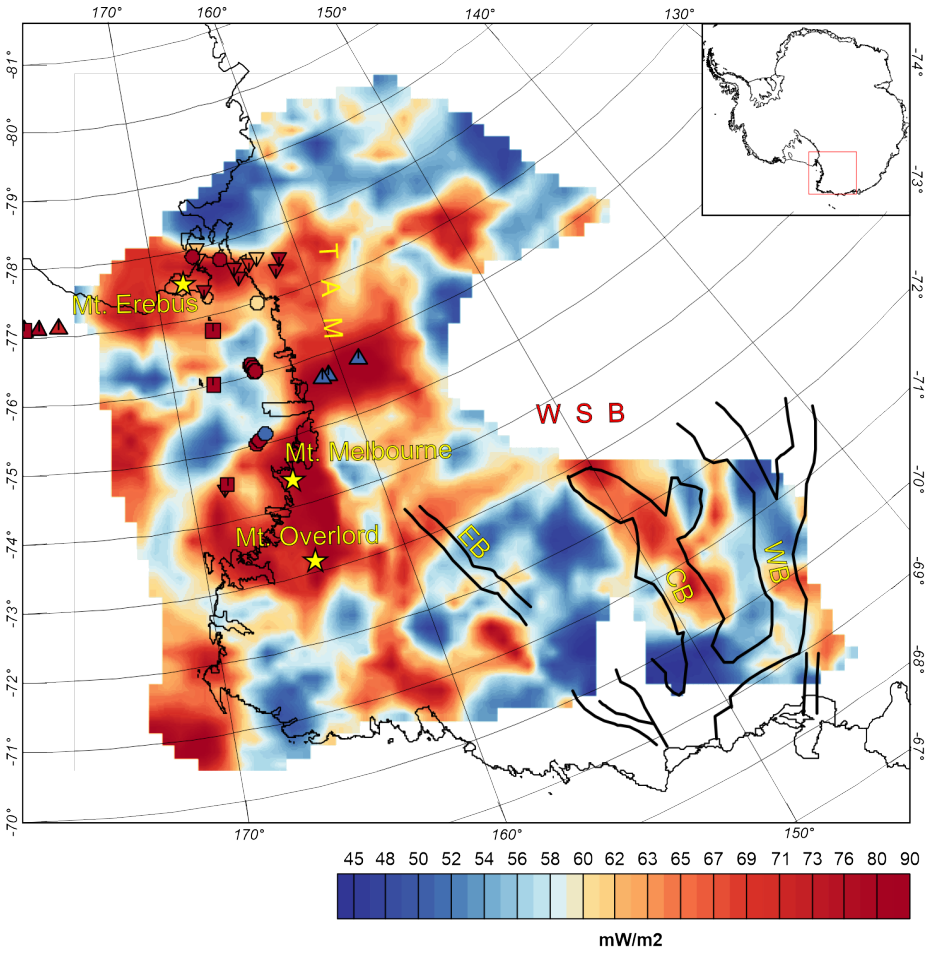

Figure 9: In situ GHF measurements [Lucazeau, 2019] superimposed on GHF estimates recovered based on an analytic window with a window size of 300 km. Circles represent A rated GHF measurements, Boxes represent B rated GHF measurements, regular triangles represent C rated GHF measurements and inverted triangles represent Z rated (not specified) rated GHF measurements. Yellow stars indicate the location of recent active volcanoes. LG, Lillie Graben; RG, Rennick Graben; EB, Eastern Basin, CB, Central Basin; WB, Western Basin; WSB, Wilkes Subglacial Basin; TAM, Transantarctic Mountains.

Difference-maps (Figure 10) between the GHF estimates based on a 300 by 300 km window to previous studies (Figure 2) show moderate differences in the order of $\pm$ 20 mW/m^2 between most models with isolated areas with stronger disagreement $\pm$ 50 mW/m^2 and more. All models predict a lower GHF beneath the southern TAM and a higher heat flow offshore. The seismic derived GHF estimates [*An et al.*, 2015; *Shen et al.*, 2020] show the least disagreement together with the statistically derived model from *Stål et al.*, [2021] to GHF estimates in

this study.

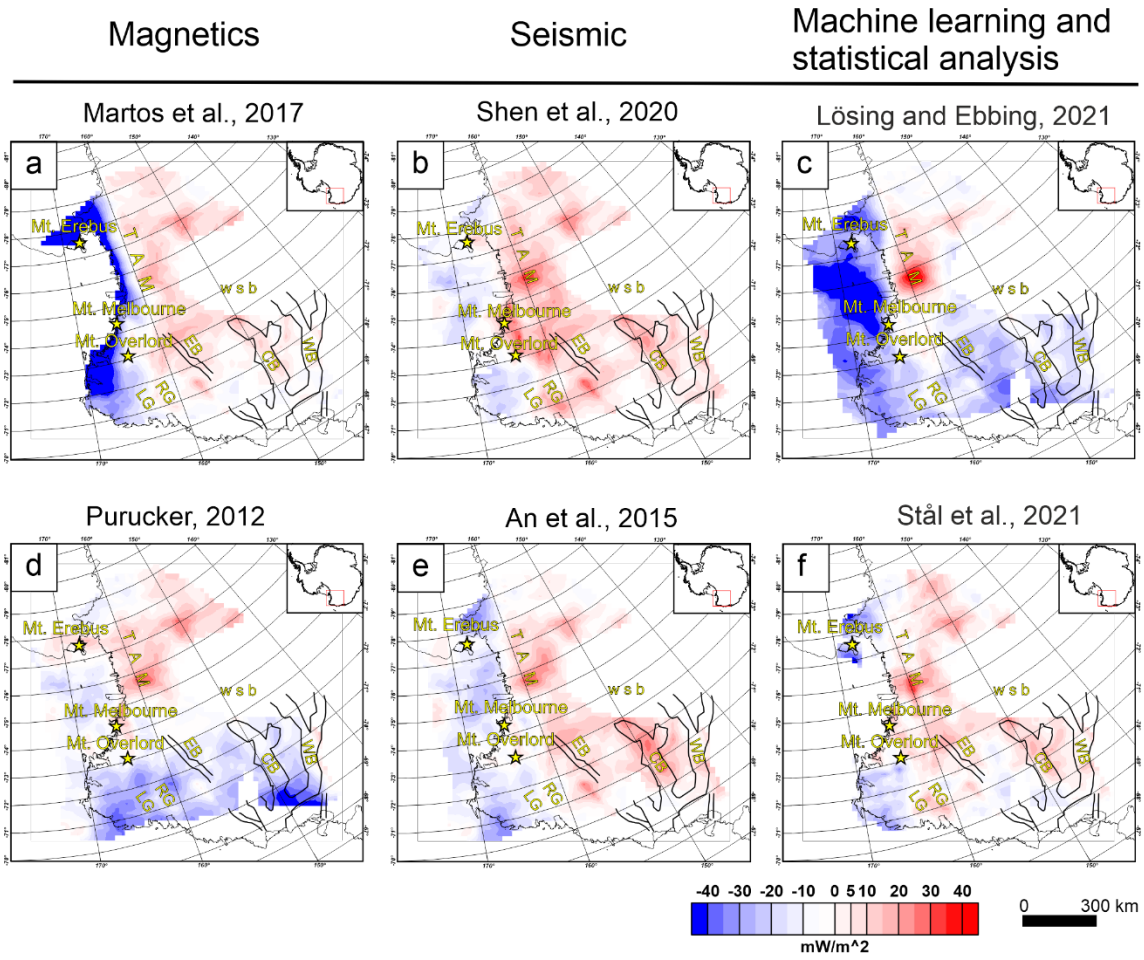

Figure 10: Difference-maps between GHF estimates of this study obtained with a window size of 300 by 300km and existing continent wide GHF models shown in Figure 2. Blue colours show lower GHF values in GHF estimates in this study, while red colours indicate higher GHF estimates in this study. a) Difference in estimated GHF values compared to [Martos et al., 2017] b) Difference in estimated GHF values compared to [Shen et al., 2020] c) Difference in estimated GHF values compared to [Lösing and Ebbing, 2021] d) Difference in estimated GHF values compared to [Purucker, 2012 an update of Fox Maule et al., 2005] e) Difference in estimated GHF values compared to [An et al., 2015] and f) Difference in estimated GHF values compared to [Stål et al., 2021].

Those three models predict GHF values in the same order of magnitude with stronger disagreements in the Rennick Graben, Central Basin and southern TAM. The GHF model derived from magnetically inferred CDP from *Martos et*

al., [2017] shows a strong disagreement at the divide to West Antarctica and a moderate disagreement in East Antarctica. The strong disagreement might be due to the fact that the *Martos et al.*, [2017] study applied different wavenumber ranges to the power spectrum to estimate the CDP for windows in West and East Antarctica, which systematically gives shallower CDP for West Antarctica and consequently results in higher heat flow. GHF prediction based on a machine learning approach by *Lösing and Ebbing*, [2021] shows strong disagreement onshore beneath the southern TAM and offshore in the Ross Sea. The much lower GHF predictions in the *Lösing and Ebbing*, [2021] model onshore beneath the TAM might be related to incorporating the three C rated GHF in situ measurements from the global GHF catalogue [*Lucazeau*, 2019]. The large difference in the Ross Sea to the *Lösing and Ebbing*, [2021] model is located where our CDP estimates exceed the Moho depth and therefore are less trustworthy.

5.3 Geological origins and implications of geothermal anomalies.

Curie depth point estimation and Geothermal heat flow predictions respectively reveal elevated heat flow beneath the northern TAM. Recently active volcanoes in the study area are: Mount Erebus, which is the southernmost active volcano on Earth [*Sims et al.*, 2021], Mount Melbourne, a quiescent volcano, which is believed to have the potential to produce major explosive events [*Gambino et al.*, 2021], and Mount Overlord, which was active during the Eocene [*Perinelli et al.*, 2017]. Those recently active volcanoes are consistent with thermal anomaly pattern of this study since each volcano is centrally located in areas of elevated heat flow (Figure 9).

The high in heat flow in the TAM region is in line with the idea of warmer West Antarctic mantle beneath the TAM providing thermal support for the mountain range as proposed by *Hansen et al.,* [2016] and the low velocity mantle imaged by recent seismic tomography models [*Lloyd et al.*, 2020; *Wiens et al.*, 2021].

A linear high heat flow anomaly is observed in the Rennick Graben. This high heat flow pattern leaks into the Lillie Graben. The opening of the Rennick Graben was previously linked to mid Cretaceous (~100 Ma) rifting and interpreted as a failed rift arm [*Fleming et al.*, 1993]. This idea is challenged by fission track data, which indicates that the Rennick Graben formed due to tectonic denudation (up to 5 km) combined with strike-slip deformation [*Rossetti et al.*, 2003]. A receiver function profile perpendicular to the Rennick Graben (Station BI01 – BI03) indicates shallow crustal thickness of 24 km [*Agostinetti et al.*, 2004]. Both mechanisms, mid Cretaceous rifting and large amount of denudation, could explain elevated heat flow in the Rennick Graben as seen in our results. Alternatively, small crustal thicknesses accompanied by a thin lithosphere can cause an elevation in heat flow. However, the thin crust imaged by receiver functions is not limited to the Rennick graben and would cause broader high heat flow patterns in contrast to the narrow heat flow pattern imaged by our results.

Another linear feature is imaged in the Central Basin (Figure 6b). Competing models of the WSB origin have been proposed in the past, including continental rifting [*Steed*, 1983], which was partially supported by airborne geophysical data [*Ferraccioli et al.*, 2001]. However, interpretation of recent aerogeophysical data suggested a rifting origin of the Central Basin is very unlikely [*Ferraccioli et al.*, 2009a; *Jordan et al.*, 2013]. Alternative models include flexural down-warp of the WSB in response to Cenozoic rift-flank uplift of the TAM caused by the neighbouring Ross Sea Rift [*Stern and ten Brink*, 1989; *ten Brink et al.*, 1997]. Similarly, a recent model proposes the WSB developed as a result of flexural processes coupled with deep glacial erosion [*Paxman et al.*, 2019]. Both mechanisms, continental Cenozoic rifting, even though unlikely, and large-scale erosion, can cause elevated heat flow and might be connected to the high heat flow pattern observed in the Central Basin. The similarity in amplitude and linear pattern of heat flow in the Rennick Graben and the Central Basin could be an indicator of a similar evolution mechanism. In the broader WSB area, except for the Rennick Graben and Central Basin the CDP and GHF maps show overall deeper and lower values, respectively, and therefore indicate a much colder thermal structure.

The CDP and consequently GHF maps from this study have a higher spatial resolution than previous continental scale GHF estimates inferred from magnetic data (Figure 2a and 2d), due to a combination of smaller distance between evaluated windows (20 km) and using only high-resolution airborne data without substituting satellite measurements. Consequently, the spatial coverage of our approach is strongly limited to the region with a dense coverage of airborne measurements.

6 Conclusion and future work

We present new CDP and GHF maps for the northern TAM and WSB area. Our spectral analysis of magnetic data provides a significant improvement over prior GHF maps of the region. We resolve elevated heat flow features in the Rennick Graben and Central Basin that have not been imaged before. However, the overall spatial coverage of this analysis is limited by the extent of airborne surveys with close flight line spacing. Filling data gaps with satellite magnetic data, as previous studies in Antarctica have done [*Dziadek et al.*, 2021; *Martos et al.*, 2017] is not an effective solution due to the wavelengths it provides for the analytic window [*Pappa and Ebbing*, 2021].

The shallow Curie depth values estimated beneath Northern Victoria Land and the TAM provide independent evidence favouring the hypothesis that warmer West Antarctica mantle provides thermal support for this part of the TAM, as imaged by seismological studies [*Hansen et al.*, 2016; *Lloyd et al.*, 2020; *Wiens et al.*, 2021]. High GHF values beneath the northern TAM and West Antarctica are also consistent with the presence of recently active volcanoes including Mount Erebus, Mount Melbourne and Mount Overlord.

Our GHF maps are a linear transformation from the CDP estimates and provide a good estimate of relative variations of the thermal structure. However, due to the high uncertainty of CDP estimates (section 5.2) and the simplified linear transformation to GHF (equation 8), absolute GHF values derived from spectral methods should be used with caution.

Despite the many assumptions and lack of onshore heat flow control data, the Curie depth and Geothermal heat flow results show convincing coherence and highlight interesting comparisons with known geological features. The approach of using exclusively high-resolution airborne data should be repeated in other areas of Antarctica with suitable magnetic data coverage to obtain relative variation in CDP.

Acknowledgements

Funding for this research was provided by NERC through a SENSE CDT studentship (NE/T00939X/1). ML acknowledges additional funding through the Gray-Milne Travel Bursary provided by the British Geophysical Association, Covid-19 Support Fund awarded by the British Geophysical Association and the Small IT grant awarded by the School of GeoSciences, The University of Edinburgh. ML acknowledges Dr. Fausto Ferraccioli for proposing the PhD project, which this research is part of, through the SENSE CDT.

The authors thank the developers of open scientific software products which were utilized in this study: Pycurious [*Mather and Delhaye*, 2019], SciPy learn [*Virtanen et al.*, 2020], NumPy [*Harris et al.*, 2020], Matplotlib [*Hunter*, 2007], Pandas [*McKinney*, 2010], Jupyter notebook [*Kluyver et al.*, 2016] as well as the developer of the commercial software Geosoft, especially the plug-in "Compudrape" and their publisher Seequent.

Open Research

CDP and GHF estimates from this study are available through the Polar data centre. In addition, power spectrum for each window and parameter of the linear regression are made publicly available for the purpose of reproducibility (link TBA). (The data is with the Polar data centre and the process of publishing the data started (providing a DOI and meta data). However, this process is delayed due to the holiday session and all the data that will be published through the Polar data centre can be accessed through this temporary link: https://www.dropbox.com/sh/p2hkn0stoqs9u56/AAAR0nICI11mlG4D7ViPMDjga?dl=0).

BedMachine Antarctica version 2 [*Morlighem et al.*, 2020] is freely available at https://nsidc.org/data/NSIDC-0756/versions/2, ADMAP-2 magnetic data [*Golynsky et al.*, 2018] is freely available at https://doi.pangaea.de/10.1594/PANGAEA.892724, The LCS-1 data [*Olsen et*

al., 2017] can be freely accessed at http://www.spacecenter.dk/files/magnetic-models/LCS-1/. GHF model from *Shen et al.,* [2020] is available at https://drive.google.com/file/d/1Fz7dAHTzPnlytuyRNctk6tAugCAjiqzR/view. GHF model from *Lösing and Ebbing,* [2021] is available from https://doi.pangaea.de/10.1594/PANGAEA.93023 GHF model from *Stål et al.,* [2021] is available at: https://doi.pangaea.de/10.1594/PANGAEA.924857. GHF model from *Martos et al., [2017]* is available at https://doi.pangaea.de/10.1594/PANGAEA.882503. GHF model from Purucker an update of Fox Maule et al., 2005 is available at http://websrv.cs.umt.edu/isis/images/c/c8/Antarctica_heat_flux_5km.nc. Heat flux map from An et al., [2015] is available at: http://www.seismolab.org/model/antarctica/lithosphere/AN1-CTD.tar.gz.

Python code in form of a Jupyter notebook to reproduce the result of this study is available at https://github.com/MaximilianLowe/CDP_GHF_TAM_WSB_JGR_solid_earth_Lowe2022.

References

https://doi.org/10.1002/2015JB011917

https://doi.org/10.1111/j.1365-2478.2005.00480.x

https://doi.org/10.1029/JB080i032p04461

https://doi.org/10.1029/JB093iB10p11817

https://doi.org/10.1029/2009JB006494

https://doi.org/10.1029/RF003p0105

https://doi.org/10.1002/ggge.20271

https://doi.org/10.1016/0040-1951(76)90023-8

https://doi.org/10.1016/j.tecto.2009.03.013

https://doi.org/10.1016/j.tecto.2008.11.028

https://doi.org/10.1016/S0012-821X(01)00459-9

https://doi.org/10.1016/j.tecto.2014.01.004

https://doi.org/10.1016/j.pepi.2020.106509

https://doi.org/10.1029/2018GL078153

https://doi.org/10.1016/j.epsl.2016.05.026

https://doi.org/10.1029/GL005i002p00105

https://doi.org/10.1002/2015JB012325

https://doi.org/10.1016/j.gsf.2017.10.012

https://doi.org/10.1016/j.geog.2017.09.006

https://doi.org/10.1016/j.tecto.2012.06.041

https://doi.org/10.1029/2012JF002371
https://doi.org/10.1029/2006GC001282
https://doi.org/10.1002/2014JB011029
https://doi.org/10.1029/2019JB017823
https://doi.org/10.1016/j.epsl.2005.10.040
https://doi.org/10.1029/2020JB021499
https://doi.org/10.1029/2019GC008389
https://doi.org/10.1002/2017GL075609
https://doi.org/10.1016/j.epsl.2012.10.018
https://doi.org/10.1029/95JB00758
https://doi.org/10.1029/2006GC001521
https://doi.org/10.1016/j.gloplacha.2003.12.005
https://doi.org/10.1029/2018GC008111
https://doi.org/10.1016/j.epsl.2010.04.025
https://doi.org/10.1029/2018GL077268
https://doi.org/10.1029/2018JF004705
https://doi.org/10.1016/j.lithos.2016.10.027
https://doi.org/10.1002/2016GL068436
https://doi.org/10.1016/j.epsl.2014.12.035
https://doi.org/10.1029/AR036p0119
https://doi.org/10.1029/2002TC001416
https://doi.org/10.1016/j.tecto.2014.04.027
https://doi.org/10.1029/2006JF000664
https://doi.org/10.1029/2017JB015346
https://doi.org/10.1029/2020GL086955
https://doi.org/10.1029/2020GC009428
https://doi.org/10.1029/JB094iB08p10315
https://doi.org/10.1016/S0012-821X(04)00066-4
https://doi.org/10.1016/S0040-1951(99)00072-4
https://doi.org/10.1029/97JB02483
https://doi.org/10.1029/91JB02231

https://doi.org/10.1016/j.pnsc.2009.07.012

https://doi.org/10.1016/j.earscirev.2010.07.003

Agostinetti, N. P., A. Amato, M. Cattaneo, and M. Di Bona (2004), Crustal structure of Northern Victoria Land from receiver function analysis., *Terra Antarctica*, *11(1)*.An, M., D. A. Wiens, Y. Zhao, M. Feng, A. Nyblade, M. Kanao, Y. Li, A. Maggi, and J.-J. Lévêque (2015), Temperature, lithosphere-asthenosphere boundary, and heat flux beneath the Antarctic Plate inferred from seismic velocities, *Journal of Geophysical Research: Solid Earth*, *120*(12), 8720-8742, doi:.Audet, P., and J. M. Gosselin (2019), Curie depth estimation from magnetic anomaly data: a re-assessment using multitaper spectral analysis and Bayesian inference, *Geophysical Journal International*, *218*(1), 494-507, doi:10.1093/gji/ggz166.Bansal, A. R., and V. P. Dimri (2005), Depth determination from a non-stationary magnetic profile for scaling geology, *Geophysical Prospecting*, *53*(3), 399-410, doi:.Bansal, A. R., G. Gabriel, V. P. Dimri, and C. M. Krawczyk (2011), Estimation of depth to the bottom of magnetic sources by a modified centroid method for fractal distribution of sources: An application to aeromagnetic data in Germany, *GEOPHYSICS*, *76*(3), L11-L22, doi:10.1190/1.3560017.Bhattacharyya, B. K., and L.-K. Leu (1975a), Analysis of magnetic anomalies over Yellowstone National Park: Mapping of Curie point isothermal surface for geothermal reconnaissance, *Journal of Geophysical Research (1896-1977)*, *80*(32), 4461-4465, doi:.Bhattacharyya, B. K., and L.-K. Leu (1975b), SPECTRAL ANALYSIS OF GRAVITY AND MAGNETIC ANOMALIES DUE TO TWO-DIMENSIONAL STRUCTURES, *GEOPHYSICS*, *40*(6), 993-1013, doi:10.1190/1.1440593.Bialas, R. W., W. R. Buck, M. Studinger, and P. G. Fitzgerald (2007), Plateau collapse model for the Transantarctic Mountains–West Antarctic Rift System: Insights from numerical experiments, *Geology*, *35*(8), 687-690, doi:10.1130/g23825a.1.Blakely, R. J. (1988), Curie temperature isotherm analysis and tectonic implications of aeromagnetic data from Nevada, *Journal of Geophysical Research: Solid Earth*, *93*(B10), 11817-11832, doi:.Blakely, R. J. (1996), *otential theory in gravity and magnetic applications*, Cambridge university press.Bouligand, C., J. M. G. Glen, and R. J. Blakely (2009), Mapping Curie temperature depth in the western United States with a fractal model for crustal magnetization, *Journal of Geophysical Research: Solid Earth*, *114*(B11), doi:.Brenn, G. R., S. E. Hansen, and Y. Park (2017), Variable thermal loading and flexural uplift along the Transantarctic Mountains, Antarctica, *Geology*, *45*(5), 463-466, doi:10.1130/g38784.1.Burton-Johnson, A., R. Dziadek, and C. Martin (2020), Review article: Geothermal heat flow in Antarctica: current and future directions, *The Cryosphere*, *14*(11), 3843-3873, doi:10.5194/tc-14-3843-2020.Clauser, C., and E. Huenges (1995), Thermal Conductivity of Rocks and Minerals, in *Rock Physics & Phase Relations*, edited, pp. 105-126, doi:.Connard, G., R. Couch, and M. Gemperle (1983), Analysis of aeromagnetic measurements from the Cascade Range in central Oregon, *GEOPHYSICS*, *48*(3), 376-390, doi:10.1190/1.1441476.Davies, J. H. (2013), Global map of solid Earth surface heat flow, *Geochemistry, Geophysics, Geosystems*, *14*(10), 4608-4622, doi:.DeConto, R. M., and D.

Pollard (2016), Contribution of Antarctica to past and future sea-level rise, *Nature*, *531*(7596), 591-597, doi:10.1038/nature17145.Drewry, D., J. (1976), Sedimentary basins of the east antarctic craton from geophysical evidence, *Tectonophysics*, *36*(1), 301-314, doi:.Dziadek, R., F. Ferraccioli, and K. Gohl (2021), High geothermal heat flow beneath Thwaites Glacier in West Antarctica inferred from aeromagnetic data, *Communications Earth & Environment*, *2*(1), 162, doi:10.1038/s43247-021-00242-3.Fahnestock, M., W. Abdalati, I. Joughin, J. Brozena, and P. Gogineni (2001), High Geothermal Heat Flow, Basal Melt, and the Origin of Rapid Ice Flow in Central Greenland, *Science*, *294*(5550), 2338-2342, doi:doi:10.1126/science.1065370.Ferraccioli, F., E. Armadillo, T. A. Jordan, E. Bozzo, and H. Corr (2009a), Aeromagnetic exploration over the East Antarctic Ice Sheet: A new view of the Wilkes Subglacial Basin, *Tectonophysics*, *478*(1), 62-77, doi:.Ferraccioli, F., E. Armadillo, A. Zunino, E. Bozzo, S. Rocchi, and P. Armienti (2009b), Magmatic and tectonic patterns over the Northern Victoria Land sector of the Transantarctic Mountains from new aeromagnetic imaging, *Tectonophysics*, *478*(1), 43-61, doi:.Ferraccioli, F., F. Coren, E. Bozzo, C. Zanolla, S. Gandolfi, I. Tabacco, and M. Frezzotti (2001), Rifted(?) crust at the East Antarctic Craton margin: gravity and magnetic interpretation along a traverse across the Wilkes Subglacial Basin region, *Earth and Planetary Science Letters*, *192*(3), 407-421, doi:.Ferré, E. C., S. A. Friedman, F. Martín-Hernández, J. M. Feinberg, J. L. Till, D. A. Ionov, and J. A. Conder (2014), Eight good reasons why the uppermost mantle could be magnetic, *Tectonophysics*, *624-625*, 3-14, doi:.Finn, C. A., J. W. Goodge, D. Damaske, and C. M. Fanning (2006), Scouting Craton's Edge in Paleo-Pacific Gondwana, in *Antarctica: Contributions to Global Earth Sciences*, edited by D. K. Fütterer, D. Damaske, G. Kleinschmidt, H. Miller and F. Tessensohn, pp. 165-173, Springer Berlin Heidelberg, Berlin, Heidelberg, doi:10.1007/3-540-32934-X_20.Fleming, T. H., D. H. Elliot, K. A. Foland, L. M. Jones, and J. R. Bowman (1993), Disturbance of Rb-Sr and K-Ar isotopic systems in the Kirkpatrick Basalt, north Victoria Land, Antarctica: implications for middle Cretaceous tectonism, *R.H. Findlay, R. Unrug, H.R. Banks, J.J. Veevers (Eds.), Gondwana Eight: Assembly, Evolution and Dispersal, Balkema, Rotterdam, 1993.*Gambino, S., P. Armienti, A. Cannata, P. Del Carlo, G. Giudice, G. Giuffrida, M. Liuzzo, and M. Pompilio (2021), Chapter 7.3 Mount Melbourne and Mount Rittmann, *Geological Society, London, Memoirs*, *55*(1), 741-758, doi:10.1144/m55-2018-43.Goes, S., D. Hasterok, D. L. Schutt, and M. Klöcking (2020), Continental lithospheric temperatures: A review, *Physics of the Earth and Planetary Interiors*, *306*, 106509, doi:.Golynsky, A. V., et al. (2018), New Magnetic Anomaly Map of the Antarctic, *Geophysical Research Letters*, *45*(13), 6437-6449, doi:.Graw, J. H., A. N. Adams, S. E. Hansen, D. A. Wiens, L. Hackworth, and Y. Park (2016), Upper mantle shear wave velocity structure beneath northern Victoria Land, Antarctica: Volcanism and uplift in the northern Transantarctic Mountains, *Earth and Planetary Science Letters*, *449*, 48-60, doi:.Haggerty, S. E. (1978), Mineralogical contraints on Curie isotherms in deep crustal magnetic anomalies, *Geophysical Research Letters*, *5*(2), 105-108, doi:.Hansen, S. E., L. M. Kenyon, J. H. Graw, Y. Park, and

A. A. Nyblade (2016), Crustal structure beneath the Northern Transantarctic Mountains and Wilkes Subglacial Basin: Implications for tectonic origins, *Journal of Geophysical Research: Solid Earth*, *121*(2), 812-825, doi:.Harris, C. R., et al. (2020), Array programming with NumPy, *Nature*, *585*(7825), 357-362, doi:10.1038/s41586-020-2649-2.Hasterok, D., M. Gard, and J. Webb (2018), On the radiogenic heat production of metamorphic, igneous, and sedimentary rocks, *Geoscience Frontiers*, *9*(6), 1777-1794, doi:.Huerta, A. D. (2007), Lithospheric Structure Across the Transantarctic Mountains Constrained by an Analysis of Gravity and Thermal Structure, *2007*(1047srp022), doi:10.3133/of2007-1047.srp022.Hunter, J. (2007), Matplotlib: A 2D Graphics Environment, *Computing in Science & Engineering*, *9*(3), 90-95, doi:doi: 10.1109/MCSE.2007.55.Hussein, M., K. Mickus, and L. F. Serpa (2013), Curie Point Depth Estimates from Aeromagnetic Data from Death Valley and Surrounding Regions, California, *Pure and Applied Geophysics*, *170*(4), 617-632, doi:10.1007/s00024-012-0557-6.Idárraga-García, J., and C. A. Vargas (2018), Depth to the bottom of magnetic layer in South America and its relationship to Curie isotherm, Moho depth and seismicity behavior, *Geodesy and Geodynamics*, *9*(1), 93-107, doi:.Jennings, S., D. Hasterok, and J. Payne (2019), A new compositionally based thermal conductivity model for plutonic rocks, *Geophysical Journal International*, *219*(2), 1377-1394, doi:10.1093/gji/ggz376.Jordan, T. A., F. Ferraccioli, E. Armadillo, and E. Bozzo (2013), Crustal architecture of the Wilkes Subglacial Basin in East Antarctica, as revealed from airborne gravity data, *Tectonophysics*, *585*, 196-206, doi:.Kluyver, T., et al. (2016), Jupyter Notebooks—a publishing format for reproducible computational workflows, *Positioning and Power in Academic Publishing: Players, Agents and Agendas, IOS Press (2016)*, 87-90.Kumar, R., A. R. Bansal, P. G. Betts, and D. Ravat (2021), Re-assessment of the depth to the base of magnetic sources (DBMS) in Australia from aeromagnetic data using the defractal method, *Geophysical Journal International*, *225*(1), 530-547, doi:10.1093/gji/ggaa601.Langel, R. A., and W. J. Hinze (1998), *The magnetic field of the Earth's lithosphere: The satellite perspective*, Cambridge University Press.Larour, E., M. Morlighem, H. Seroussi, J. Schiermeier, and E. Rignot (2012), Ice flow sensitivity to geothermal heat flux of Pine Island Glacier, Antarctica, *Journal of Geophysical Research: Earth Surface*, *117*(F4), doi:.Lawrence, J. F., D. A. Wiens, A. A. Nyblade, S. Anandakrishnan, P. J. Shore, and D. Voigt (2006), Crust and upper mantle structure of the Transantarctic Mountains and surrounding regions from receiver functions, surface waves, and gravity: Implications for uplift models, *Geochemistry, Geophysics, Geosystems*, *7*(10), doi:.Leseane, K., E. A. Atekwana, K. L. Mickus, M. G. Abdelsalam, E. M. Shemang, and E. A. Atekwana (2015), Thermal perturbations beneath the incipient Okavango Rift Zone, northwest Botswana, *Journal of Geophysical Research: Solid Earth*, *120*(2), 1210-1228, doi:.Li, C.-F., Y. Lu, and J. Wang (2017), A global reference model of Curie-point depths based on EMAG2, *Scientific Reports*, *7*(1), 45129, doi:10.1038/srep45129.Li, C.-F., D. Zhou, and J. Wang (2019), On application of fractal magnetization in Curie depth estimation from magnetic anomalies, *Acta Geophysica*, *67*(5), 1319-1327, doi:10.1007/s11600-019-00339-6.Lloyd, A.

J., et al. (2020), Seismic Structure of the Antarctic Upper Mantle Imaged with Adjoint Tomography, *Journal of Geophysical Research: Solid Earth*, *125*(3), doi:.Llubes, M., C. Lanseau, and F. Rémy (2006), Relations between basal condition, subglacial hydrological networks and geothermal flux in Antarctica, *Earth and Planetary Science Letters*, *241*(3), 655-662, doi:.Lösing, M., and J. Ebbing (2021), Predicting Geothermal Heat Flow in Antarctica With a Machine Learning Approach, *Journal of Geophysical Research: Solid Earth*, *126*(6), e2020JB021499, doi:.Lösing, M., J. Ebbing, and W. Szwillus (2020), Geothermal Heat Flux in Antarctica: Assessing Models and Observations by Bayesian Inversion, *Frontiers in Earth Science*, *8*, doi:10.3389/feart.2020.00105.Lucazeau, F. (2019), Analysis and Mapping of an Updated Terrestrial Heat Flow Data Set, *Geochemistry, Geophysics, Geosystems*, *20*(8), 4001-4024, doi:.Martos, Y. M., M. Catalán, T. A. Jordan, A. Golynsky, D. Golynsky, G. Eagles, and D. G. Vaughan (2017), Heat Flux Distribution of Antarctica Unveiled, *Geophysical Research Letters*, *44*(22), 11,417-411,426, doi:.Mather, B., and R. Delhaye (2019), PyCurious: A Python module for computing the Curie depth from the magnetic anomaly, *Journal of Open Source Software*, *4*(39), doi:10.21105/joss.01544.Mather, B., and J. Fullea (2019), Constraining the geotherm beneath the British Isles from Bayesian inversion of Curie depth: integrated modelling of magnetic, geothermal, and seismic data, *Solid Earth*, *10*(3), 839-850, doi:10.5194/se-10-839-2019.Matsuoka, K., J. A. MacGregor, and F. Pattyn (2012), Predicting radar attenuation within the Antarctic ice sheet, *Earth and Planetary Science Letters*, *359-360*, 173-183, doi:.Maus, S., and V. Dimri (1995), Potential field power spectrum inversion for scaling geology, *Journal of Geophysical Research: Solid Earth*, *100*(B7), 12605-12616, doi:.Maus, S., D. Gordon, and D. Fairhead (1997), Curie-temperature depth estimation using a self-similar magnetization model, *Geophysical Journal International*, *129*(1), 163-168, doi:10.1111/j.1365-246X.1997.tb00945.x.Maus, S., H. Lühr, M. Rother, K. Hemant, G. Balasis, P. Ritter, and C. Stolle (2007), Fifth-generation lithospheric magnetic field model from CHAMP satellite measurements, *Geochemistry, Geophysics, Geosystems*, *8*(5), doi:.McKinney, W. (2010), Data structures for statistical computing in python, *Proceedings of the 9th Python in Science Conference*, *445*(1), 51-56.Morelli, A., and S. Danesi (2004), Seismological imaging of the Antarctic continental lithosphere: a review, *Global and Planetary Change*, *42*(1), 155-165, doi:.Morlighem, M., et al. (2020), Deep glacial troughs and stabilizing ridges unveiled beneath the margins of the Antarctic ice sheet, *Nature Geoscience*, *13*(2), 132-137, doi:10.1038/s41561-019-0510-8.Núñez Demarco, P., C. Prezzi, and L. Sánchez Bettucci (2020), Review of Curie point depth determination through different spectral methods applied to magnetic data, *Geophysical Journal International*, *224*(1), 17-39, doi:10.1093/gji/ggaa361.Okubo, Y., R. J. Graf, R. O. Hansen, K. Ogawa, and H. Tsu (1985), Curie point depths of the Island of Kyushu and surrounding areas, Japan, *GEOPHYSICS*, *50*(3), 481-494, doi:10.1190/1.1441926.Olsen, N., D. Ravat, C. C. Finlay, and L. K. Kother (2017), LCS-1: a high-resolution global model of the lithospheric magnetic field derived from CHAMP and Swarm satellite observations, *Geophysical Journal*

International, *211*(3), 1461-1477, doi:10.1093/gji/ggx381.Pappa, F., and J. Ebbing (2021), Gravity, magnetics and geothermal heat flow of the Antarctic lithospheric crust and mantle, *Geological Society, London, Memoirs*, *56*, M56-2020-2025, doi:10.1144/m56-2020-5.Pappa, F., J. Ebbing, and F. Ferraccioli (2019), Moho Depths of Antarctica: Comparison of Seismic, Gravity, and Isostatic Results, *Geochemistry, Geophysics, Geosystems*, *20*(3), 1629-1645, doi:.Pattyn, F. (2010), Antarctic subglacial conditions inferred from a hybrid ice sheet/ice stream model, *Earth and Planetary Science Letters*, *295*(3), 451-461, doi:.Pattyn, F., S. P. Carter, and M. Thoma (2016), Advances in modelling subglacial lakes and their interaction with the Antarctic ice sheet, *Philosophical Transactions of the Royal Society A: Mathematical, Physical and Engineering Sciences*, *374*(2059), 20140296, doi:doi:10.1098/rsta.2014.0296.Paxman, G. J. G., S. S. R. Jamieson, F. Ferraccioli, M. J. Bentley, N. Ross, E. Armadillo, E. G. W. Gasson, G. Leitchenkov, and R. M. DeConto (2018), Bedrock Erosion Surfaces Record Former East Antarctic Ice Sheet Extent, *Geophysical Research Letters*, *45*(9), 4114-4123, doi:.Paxman, G. J. G., S. S. R. Jamieson, F. Ferraccioli, M. J. Bentley, N. Ross, A. B. Watts, G. Leitchenkov, E. Armadillo, and D. A. Young (2019), The Role of Lithospheric Flexure in the Landscape Evolution of the Wilkes Subglacial Basin and Transantarctic Mountains, East Antarctica, *Journal of Geophysical Research: Earth Surface*, *124*(3), 812-829, doi:.Perinelli, C., M. Gaeta, and P. Armienti (2017), Cumulate xenoliths from Mt. Overlord, northern Victoria Land, Antarctica: A window into high pressure storage and differentiation of mantle-derived basalts, *Lithos*, *268-271*, 225-239, doi:.Pittard, M. L., B. K. Galton-Fenzi, J. L. Roberts, and C. S. Watson (2016), Organization of ice flow by localized regions of elevated geothermal heat flux, *Geophysical Research Letters*, *43*(7), 3342-3350, doi:.Pollard, D., R. M. DeConto, and R. B. Alley (2015), Potential Antarctic Ice Sheet retreat driven by hydrofracturing and ice cliff failure, *Earth and Planetary Science Letters*, *412*, 112-121, doi:.Purucker, M.: Geothermal heat flux data set based on low resolution observations collected by the CHAMP satellite between 2000 and 2010, and produced from the MF-6 model following the technique described in Fox Maule et al. (2005), available at: http://websrv.cs.umt.edu/isis/images/c/c8/Antarctica_heat_flux_5km.nc (last access: 11 August 2022), 2012.Ravat, D., A. Pignatelli, I. Nicolosi, and M. Chiappini (2007), A study of spectral methods of estimating the depth to the bottom of magnetic sources from near-surface magnetic anomaly data, *Geophysical Journal International*, *169*(2), 421-434, doi:10.1111/j.1365-246X.2007.03305.x.Robinson, E. S., and J. F. Splettstoesser (1986), Structure of the Transantarctic Mountains Determined From Geophysical Surveys, in *Geology of the Central Transantarctic Mountains*, edited, pp. 119-162, doi:.Rossetti, F., F. Lisker, F. Storti, and A. L. Läufer (2003), Tectonic and denudational history of the Rennick Graben (North Victoria Land): Implications for the evolution of rifting between East and West Antarctica, *Tectonics*, *22*(2), doi:.Salem, A., C. Green, D. Ravat, K. H. Singh, P. East, J. D. Fairhead, S. Mogren, and E. Biegert (2014), Depth to Curie temperature across the central Red Sea from magnetic data using the de-fractal method, *Tectonophysics*,

624-625, 75-86, doi:.Schoof, C. (2007), Ice sheet grounding line dynamics: Steady states, stability, and hysteresis, *Journal of Geophysical Research: Earth Surface*, *112*(F3), doi:.Shen, W., et al. (2018), The Crust and Upper Mantle Structure of Central and West Antarctica From Bayesian Inversion of Rayleigh Wave and Receiver Functions, *Journal of Geophysical Research: Solid Earth*, *123*(9), 7824-7849, doi:.Shen, W., D. A. Wiens, A. J. Lloyd, and A. A. Nyblade (2020), A Geothermal Heat Flux Map of Antarctica Empirically Constrained by Seismic Structure, *Geophysical Research Letters*, *47*(14), e2020GL086955, doi:.Sims, K. W. W., R. C. Aster, G. Gaetani, J. Blichert-Toft, E. H. Phillips, P. J. Wallace, G. S. Mattioli, D. Rasmussen, and E. S. Boyd (2021), Chapter 7.2 Mount Erebus, *Geological Society, London, Memoirs*, *55*(1), 695-739, doi:10.1144/m55-2019-8.Smith, A. G., and D. J. Drewry (1984), Delayed phase change due to hot asthenosphere causes Transantarctic uplift?, *Nature*, *309*(5968), 536-538, doi:10.1038/309536a0.Spector, A., and F. S. Grant (1970), STATISTICAL MODELS FOR INTERPRETING AEROMAGNETIC DATA, *GEOPHYSICS*, *35*(2), 293-302, doi:10.1190/1.1440092.Stål, T., A. M. Reading, J. A. Halpin, and J. M. Whittaker (2021), Antarctic Geothermal Heat Flow Model: Aq1, *Geochemistry, Geophysics, Geosystems*, *22*(2), e2020GC009428, doi:.Steed, R. N. (1983), Structural interpretations of Wilkes Land, Antarctica, *Antarctic earth science. International symposium*, *4*.Stern, T. A., and U. ten Brink, S. (1989), Flexural uplift of the Transantarctic Mountains, *Journal of Geophysical Research: Solid Earth*, *94*(B8), 10315-10330, doi:.Stokes, C. R., et al. (2022), Response of the East Antarctic Ice Sheet to past and future climate change, *Nature*, *608*(7922), 275-286, doi:10.1038/s41586-022-04946-0.Studinger, M., R. E. Bell, W. R. Buck, G. D. Karner, and D. D. Blankenship (2004), Sub-ice geology inland of the Transantarctic Mountains in light of new aerogeophysical data, *Earth and Planetary Science Letters*, *220*(3), 391-408, doi:.Tanaka, A., Y. Okubo, and O. Matsubayashi (1999), Curie point depth based on spectrum analysis of the magnetic anomaly data in East and Southeast Asia, *Tectonophysics*, *306*(3), 461-470, doi:.Telford, W. M., L. P. Geldart, and R. E. Sheriff (1990), *Applied Geophysics*, Cambridge University Press.ten Brink, U., S., R. I. Hackney, S. Bannister, T. A. Stern, and Y. Makovsky (1997), Uplift of the Transantarctic Mountains and the bedrock beneath the East Antarctic ice sheet, *Journal of Geophysical Research: Solid Earth*, *102*(B12), 27603-27621, doi:.ten Brink, U., S., and T. Stern (1992), Rift flank uplifts and Hinterland Basins: Comparison of the Transantarctic Mountains with the Great Escarpment of southern Africa, *Journal of Geophysical Research: Solid Earth*, *97*(B1), 569-585, doi:.Todoeschuck, J. P., M. Pilkington, and M. E. Gregotski (1992), If geology is fractal, what do we do next?, *The Leading Edge*, *11*(10), 29-35, doi:10.1190/1.1436848.Treitel, S., W. G. Clement, and R. K. Kaul (1971), The Spectral Determination of Depths to Buried Magnetic Basement Rocks, *Geophysical Journal International*, *24*(4), 415-428, doi:10.1111/j.1365-246X.1971.tb02187.x.Turcotte, D. L., and G. Schubert (2002), *Geodynamics*, Cambridge university press.Van Liefferinge, B., F. Pattyn, M. G. P. Cavitte, N. B. Karlsson, D. A. Young, J. Sutter, and O. Eisen (2018), Promising Oldest Ice sites in East Antarctica based on thermodynamical modelling, *The*

Cryosphere, *12*(8), 2773-2787, doi:10.5194/tc-12-2773-2018.Virtanen, P., et al. (2020), SciPy 1.0: fundamental algorithms for scientific computing in Python, *Nature Methods*, *17*(3), 261-272, doi:10.1038/s41592-019-0686-2.Wang, Y., and S. Hou (2009), A new interpolation method for Antarctic surface temperature, *Progress in Natural Science*, *19*(12), 1843-1849, doi:.Wannamaker, P., et al. (2017), Uplift of the central transantarctic mountains, *Nature Communications*, *8*(1), 1588, doi:10.1038/s41467-017-01577-2.Whitehouse, P. L., N. Gomez, M. A. King, and D. A. Wiens (2019), Solid Earth change and the evolution of the Antarctic Ice Sheet, *Nature Communications*, *10*(1), 503, doi:10.1038/s41467-018-08068-y.Wiens, D. A., W. Shen, and A. J. Lloyd (2021), The seismic structure of the Antarctic upper mantle, *Geological Society, London, Memoirs*, *56*, M56-2020-2018, doi:10.1144/m56-2020-18.Winkelmann, R., M. A. Martin, M. Haseloff, T. Albrecht, E. Bueler, C. Khroulev, and A. Levermann (2011), The Potsdam Parallel Ice Sheet Model (PISM-PIK) – Part 1: Model description, *The Cryosphere*, *5*(3), 715-726, doi:10.5194/tc-5-715-2011.Winsborrow, M. C. M., C. D. Clark, and C. R. Stokes (2010), What controls the location of ice streams?, *Earth-Science Reviews*, *103*(1), 45-59, doi:.Yamasaki, T., H. Miura, and Y. Nogi (2008), Numerical modelling study on the flexural uplift of the Transantarctic Mountains, *Geophysical Journal International*, *174*(1), 377-390, doi:10.1111/j.1365-246X.2008.03815.x.

Journal of

Journal of Geophysical Research: Solid Earth

Supporting Information for

Anomalously high heat flow regions beneath the Transantarctic Mountains and Wilkes Subglacial Basin in East Antarctica inferred from Curie depth

Maximilian Low[e1,2], Ben Mather[3], Chris Green[4], Tom A. Jordan[1], Jörg Ebbing[5], Robert Larter[1]

[1]British Antarctic Survey, Cambridge, United Kingdom.

[2]The University of Edinburgh, Edinburgh, United Kingdom.

[3]The University of Sydney, Sydney, Australia.

[4]University of Leeds, Leeds, United Kingdom.

[5]Christian-Albrechts-Universität zu Kiel, Kiel, Germany.

Contents of this file

Introduction

This supporting information files provides information on the upward continuation of the magnetic data in S1, the effect of steps size between the windows in S2, a sensitivity test of a dry ice sheet base scenario and ice-free scenario in S3 as well as illustrates the effect of varying wavenumber range on the CDP estimation in S4.

S1 Upward continuation

The selected magnetic data from ADMAP-2 (Figure S1a) was upward continued using the Compudrape extension of Geosoft. In order to perform the upward continuation of the

magnetic data an elevation grid is required containing the flight height of the magnetic measurements (Figure S2b). This elevation grid was produced by gridding the flight heights reported in the ADMAP-2 database. The magnetic data was then upward continued to a constant elevation of 4000 m, which corresponds to the highest flight altitude of the magnetic surveys.

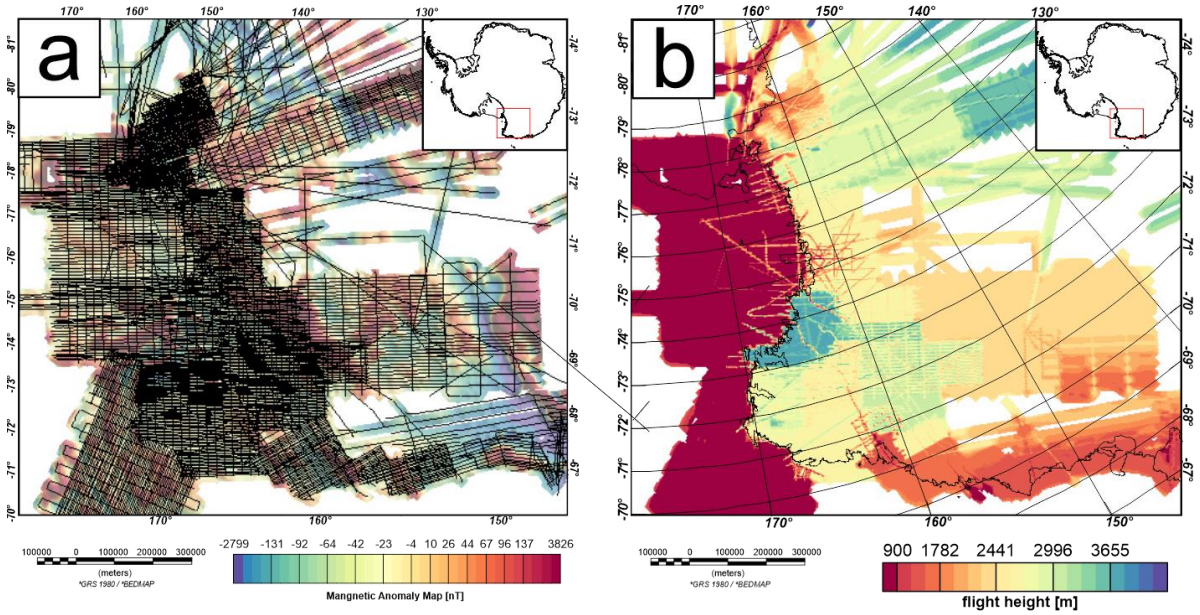

Figure S1. a) flight lines of selected ADMAP-2 data superimposed on ADMAP-2 magnetic data. b) flight height grid for upward continuation.

S2 Shifting windows

The spacing between the windows in which the radially averaged power spectrum is calculated has a considerable influence on the high frequency variation within the CDP map and consequently the GHF map. A larger window spacing will result in a smoother map of CDP and GHF estimates. This effect is illustrated in Figure S2. Here, window spacing of 50 km (Figure S2a) is compared to a window spacing of 20 km (Figure S2b). Both estimates are based on a window size of 300 km. The GHF map inferred from a 50 km window spacing is considerably smoother. Nevertheless, the main GHF features are present in both maps

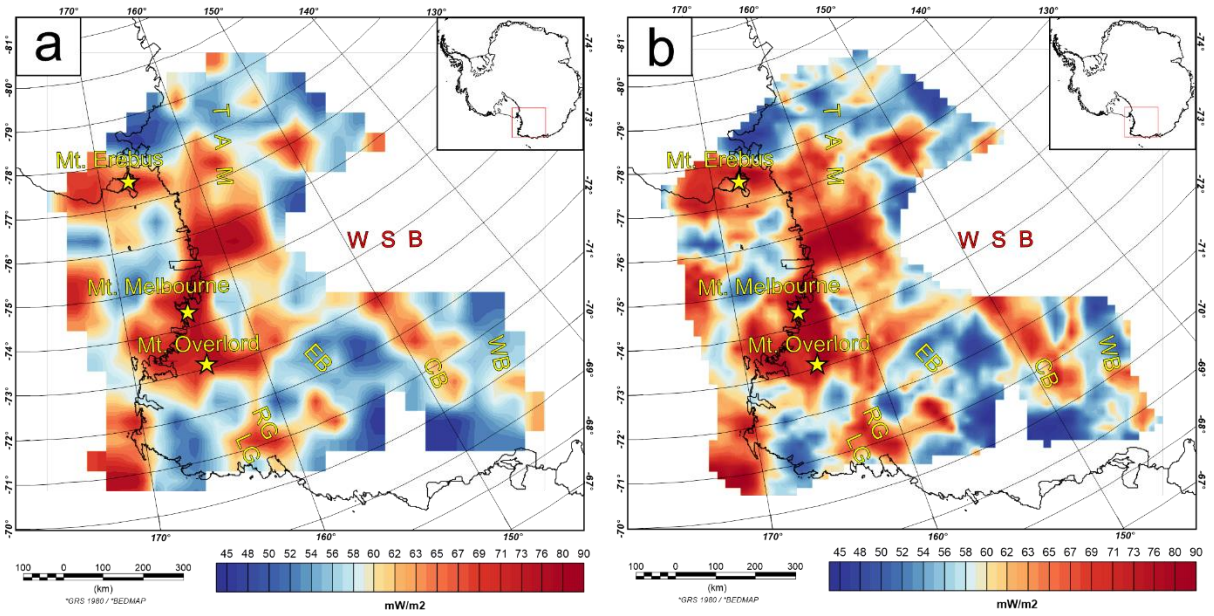

Figure S2. a) GHF estimates based on a window spacing of 50 km b) GHF estimates based on a window spacing of 20 km. LG, Lillie Graben; RG, Rennick Graben; EB, Eastern Basin, CB, Central Basin; WB, Western Basin; WBS, Wilkes Subglacial Basin; TAM, Transantarctic Mountains.

S3 Dry base ice sheet and ice-free scenario

Surface temperatures are assumed to be 0 °C in equation 8. This assumption assumes a wet base of the ice sheet close to the pressure melting point of -2 °C ± a few degrees. However, temperatures are significantly lower if the base of the ice sheet is dry, or no ice cover is present. In such scenario the ice surface temperature is closer to the annual mean temperature. We performed a sensitivity test for a dry base scenario assuming a surface temperature of -30 degrees. The difference between a wet and dry base scenario is between 3 and 6 mW/m^2, which is below the uncertainty of GHF inferred from Curie depth points (Figure S3).

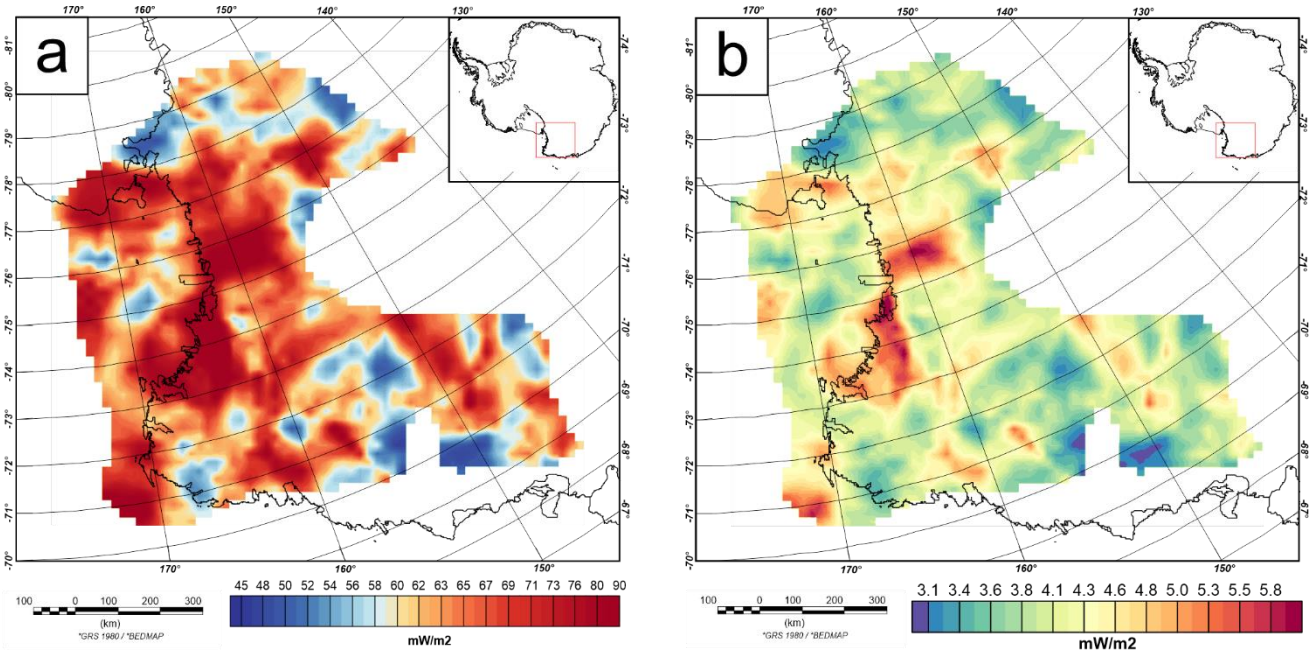

Figure S3. a) GHF estimates with a surface temperature of -30 °C for an ice sheet with a dry base or ice-free scenario. b) Difference between GHF estimates using ice surface temperature of -30 °C representing dry base of the icesheet and ice-free scenario and bedrock surface temperature of 0 °C representing an ice sheet with a wet base.

S4 Wavenumber variation

Selecting the correct wavenumber range to estimate Z_0 and Z_t is crucial for the estimation of the bottom of magnetic source which is interpreted as the Curie depth point. Varying the low wavenumber range (long wavelength content) can change the result for Z_0 by several km (Figures S4 – S13). Including or excluding one data point in the low wavenumber part of the power spectrum results in a variation of Z_0 estimation of a few km (Figure S4 b-d, S8 b-d, S10 b-d, S12 b-d). Equation 6 (main manuscript) states that Z_0 is multiplied by two. Therefore, the uncertainty which originates from a poorly selected wavenumber range for Z_0 is magnified. The low wavenumber content between the different windows does not vary significantly in our study and hence a suitable wavenumber range for Z_0 can be identified and selected by inspecting power spectra from different windows (Figures S4, S6, S8, S10, S12). The high wavenumber content differs strongly for different windows in our study (Figures S5, S7, S9, S11, S13). However, the influence of different wavenumber ranges has only a little effect on the Z_t estimation (Figures S5 b-d, S7 b-d, S9 b-d, S11 b-d, S13 b-d). Including or excluding a

large portion of data points to estimate Z_t results only in a variation of roughly 300 meters (Figure 12 b-d). In contrast to Z_0 the Z_t value is not multiplied in equation 6 and is therefore overall, less dominant then the Z_0 value to estimate the CDP. Using a constant wavenumber range for all windows in an automated process is robust because i) the low wavenumber range to estimate Z_0 is very stable, and a suitable wavenumber range can be selected and ii) the strong variation in the high wavenumber range is negligible since choosing a wrong wavenumber range (Figures S5, S7, S9, S11, S13) results in a variation of the CDP below the formal uncertainty. In other words, the method is not sensitive to variation in a sub km scale.

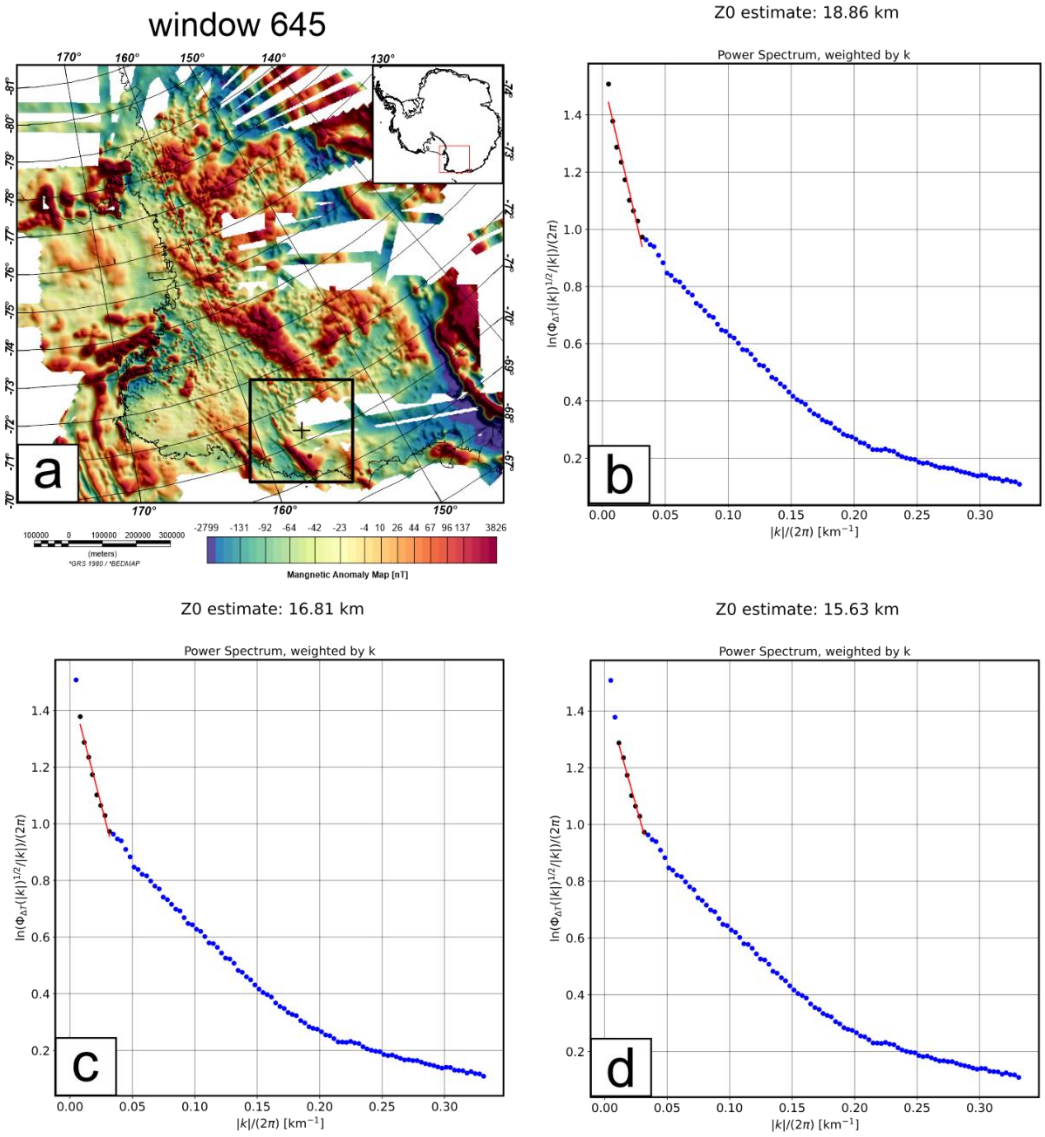

Figure S4. a) Power spectrum from window 645 with a window size of 300 km. Blue dots power spectrum data points. Black dots indicate data points used for the linear regression. Red line

linear fit to estimate Z_0 a) Window location and extent superimposed on magnetic data. b) wavenumber range 0 – 0.033 |k|/2π, Z_0 estimate: 18.86 km. c) wavenumber range wavenumber range 0.006 – 0.033 |k|/2π, Z_0 estimate: 16.91 km. d) wavenumber range 0.01 – 0.033 |k|/2π, Z_0 estimate: 15.63 km.

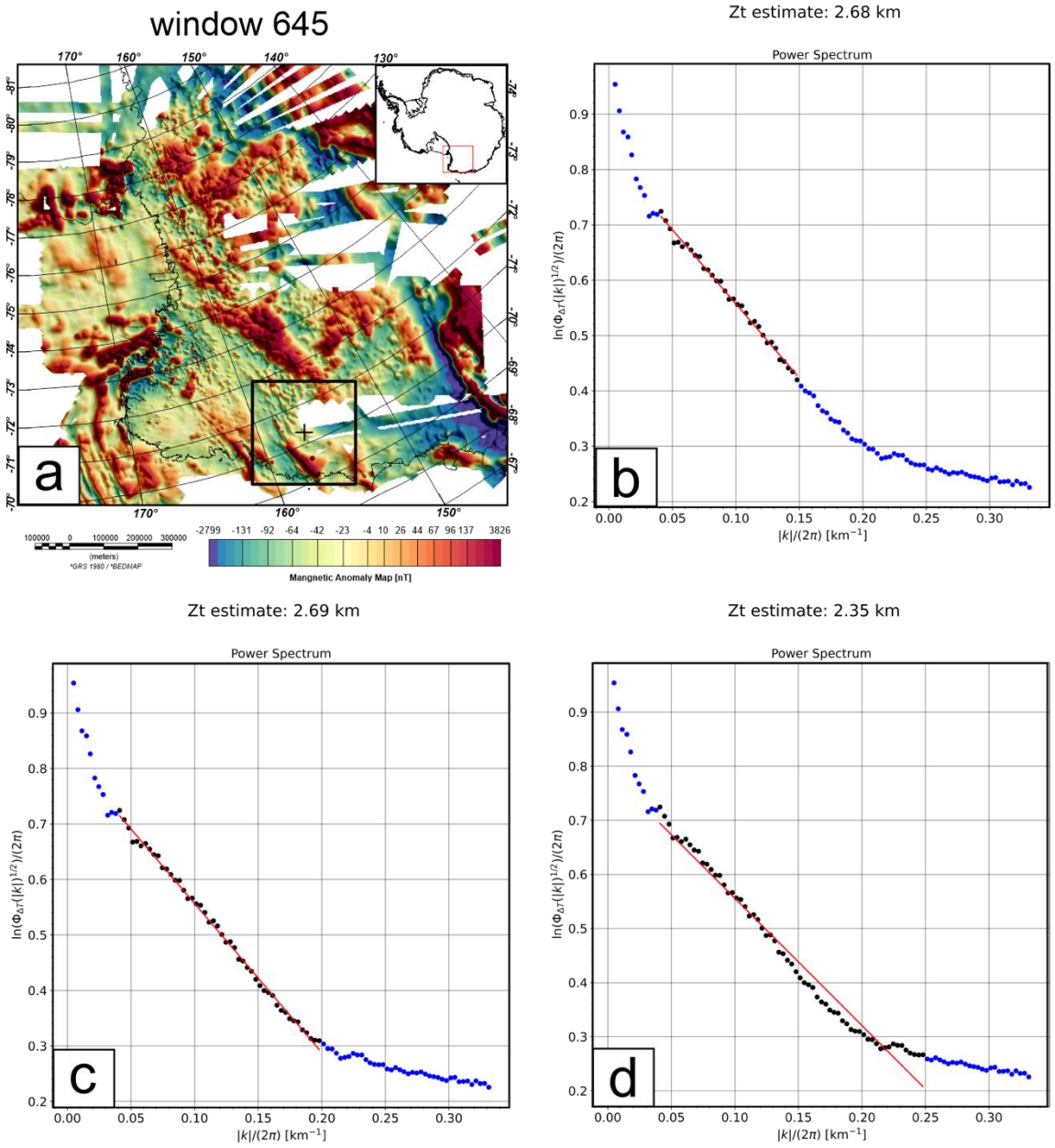

Figure S5. Power spectrum from window 645 with a window size of 300 km. Blue dots power spectrum data points. Black dots indicate data points used for the linear regression. Red line linear fit to estimate Z_0. a) Window location and extent superimposed on magnetic data. b)

wavenumber range 0.04 – 0.25 |k|/2π, Z_t estimate: 2.68 km. c) wavenumber range 0.04 – 0.2 |k|/2π, Z_t estimate: 2.69 km d) wavenumber range 0.04 – 0.15 |k|/2π, Z_t estimate: 2.35 km.

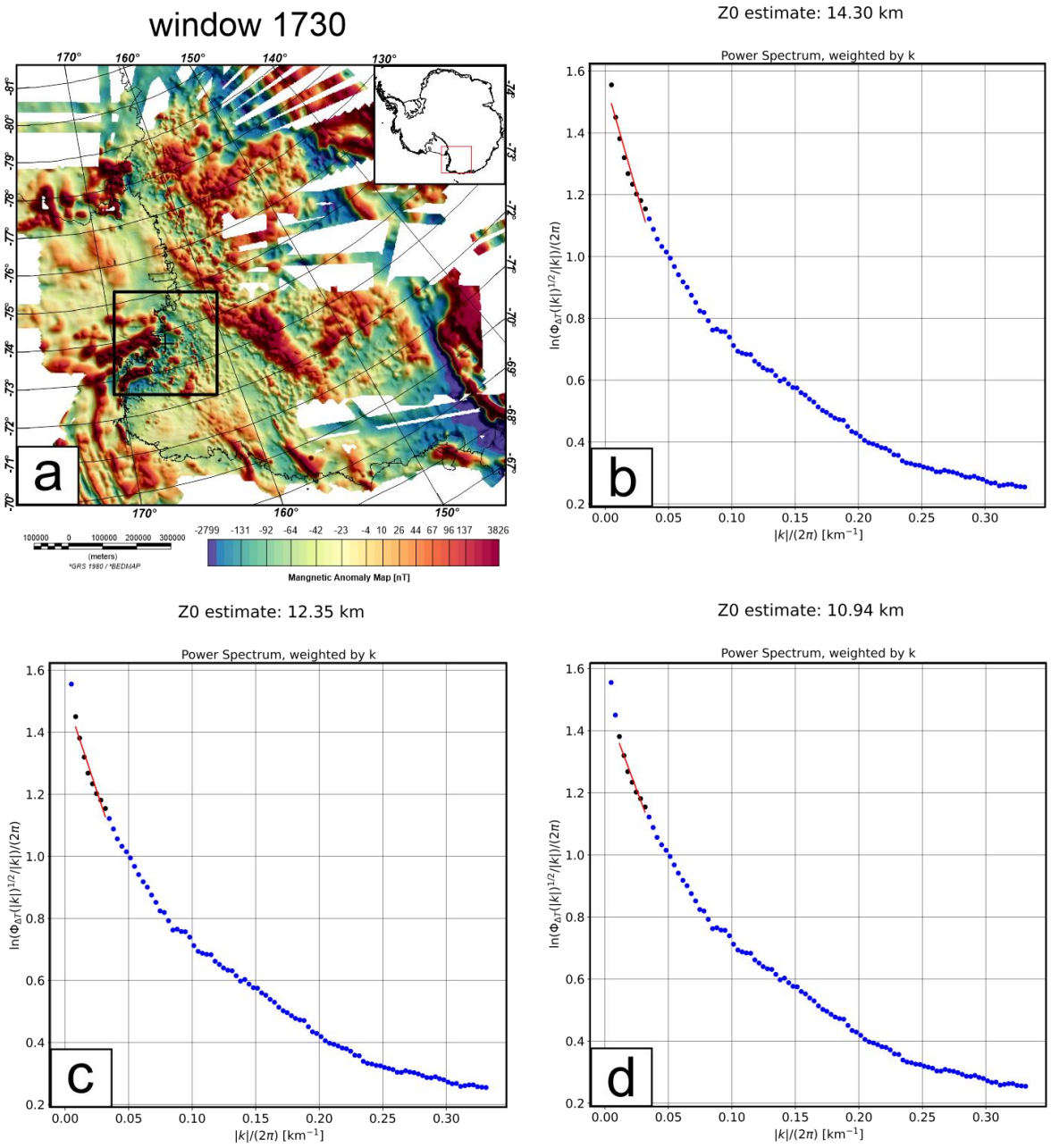

Figure S6. Power spectrum from window 1730 with a window size of 300 km. Blue dots power spectrum data points. Black dots indicate data points used for the linear regression. Red line linear fit to estimate Z0 a) Window location and extent superimposed on magnetic data. b) wavenumber range 0 – 0.033 |k|/2π, Z0 estimate: 14.3 km. c) wavenumber range wavenumber range 0.006 – 0.033 |k|/2π, Z0 estimate: 12.35 km. d) wavenumber range 0.01 – 0.033 |k|/2π, Z0 estimate: 10.94 km.

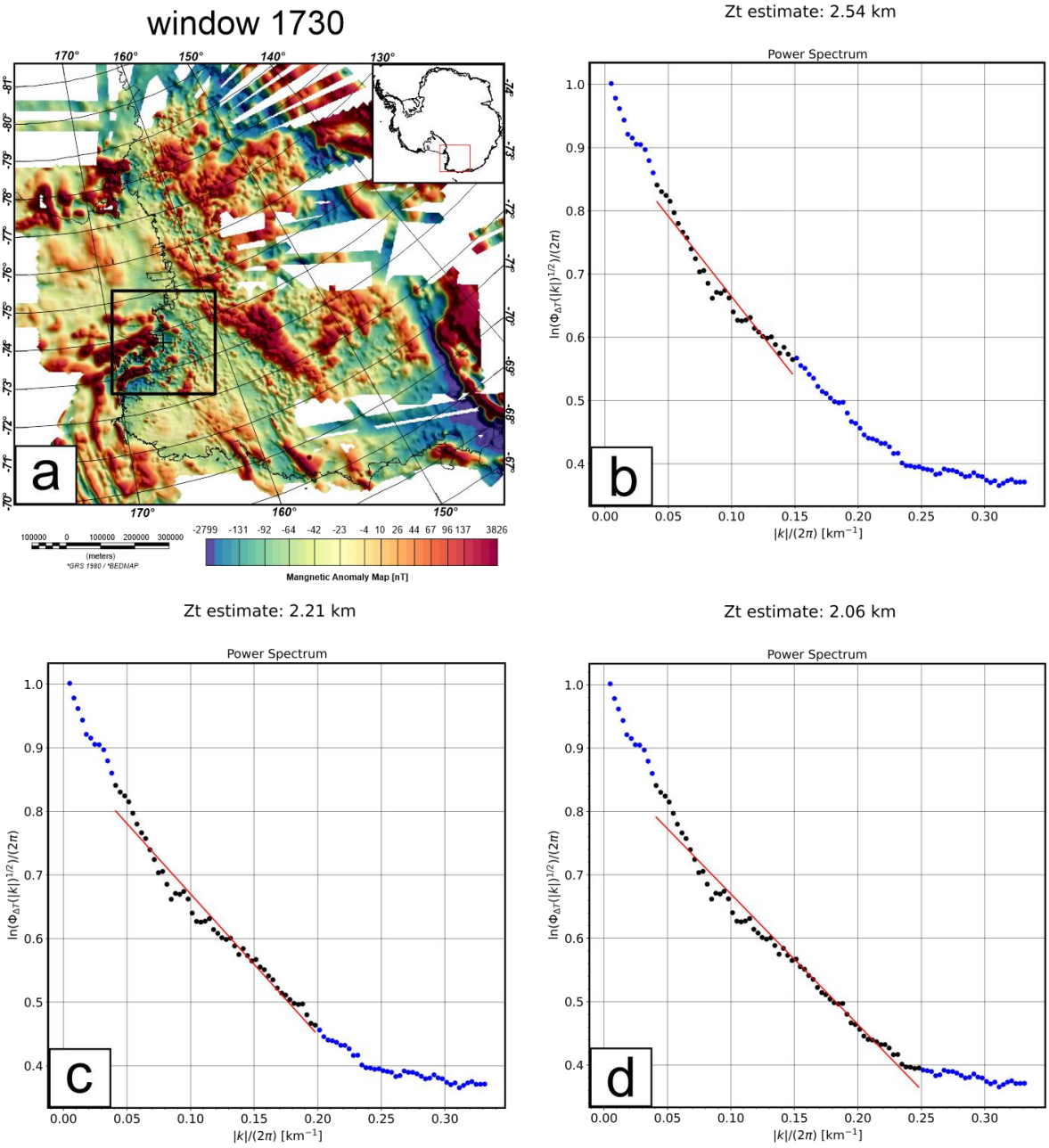

Figure S7. Power spectrum from window 645 with a window size of 300 km. Blue dots power spectrum data points. Black dots indicate data points used for the linear regression. Red line linear fit to estimate Z0. a) Window location and extent superimposed on magnetic data. b)

wavenumber range 0.04 – 0.25 |k|/2π, Zt estimate: 2.54 km. c) wavenumber range 0.04 – 0.2 |k|/2π, Zt estimate: 2.21 d) wavenumber range 0.04 – 0.15 |k|/2π, Zt estimate: 2.06 km.

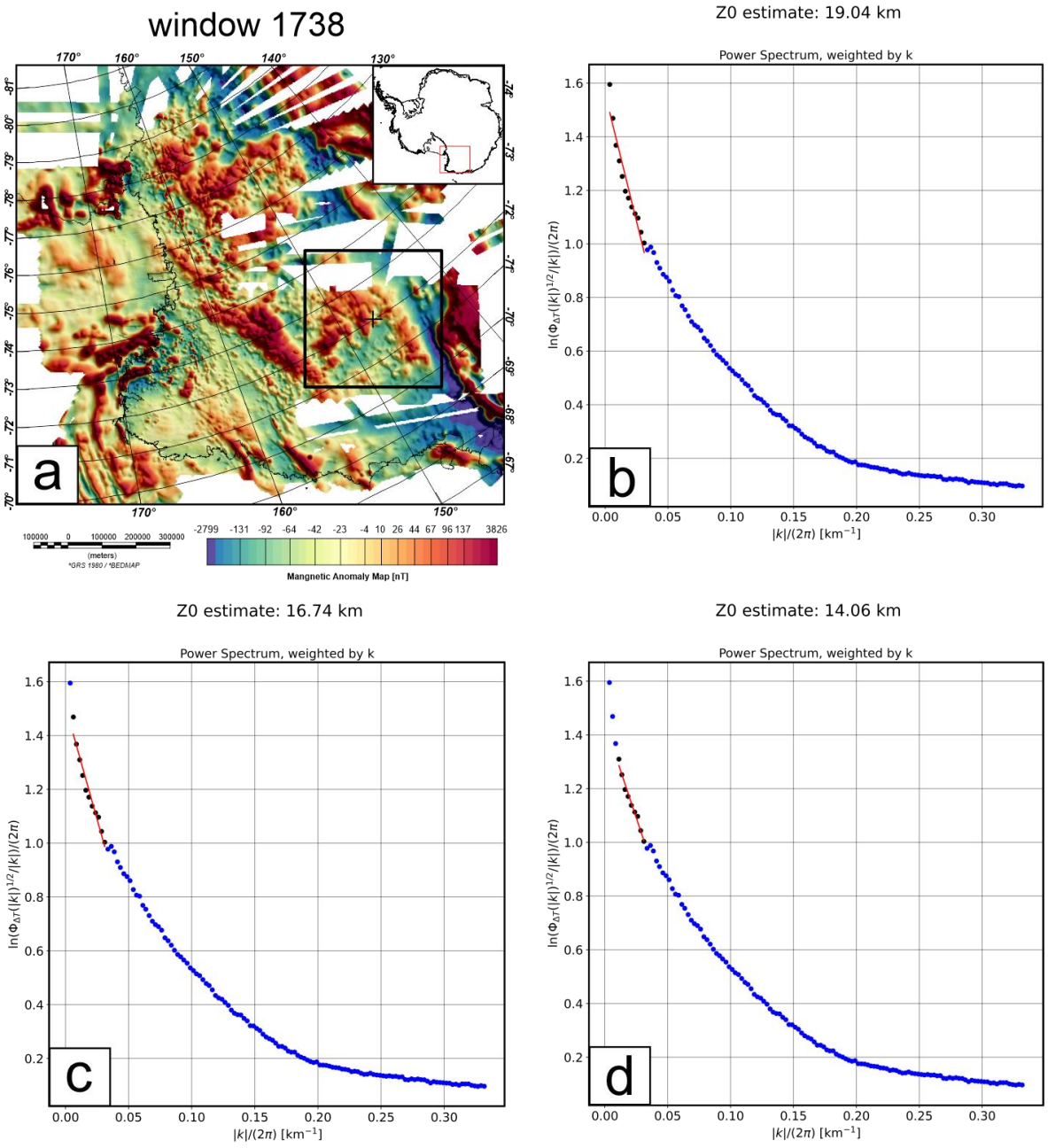

Figure S8. Power spectrum from window 1730 with a window size of 400 km. Blue dots power spectrum data points. Black dots indicate data points used for the linear regression. Red line linear fit to estimate Z0 a) Window location and extent superimposed on magnetic data. b) wavenumber range 0 – 0.033 |k|/2π, Z0 estimate: 19.04 km. c) wavenumber range wavenumber

range 0.006 – 0.033 |k|/2π, Z0 estimate: 16.74 km. d) wavenumber range 0.01 – 0.033 |k|/2π, Z0 estimate: 14.06 km.

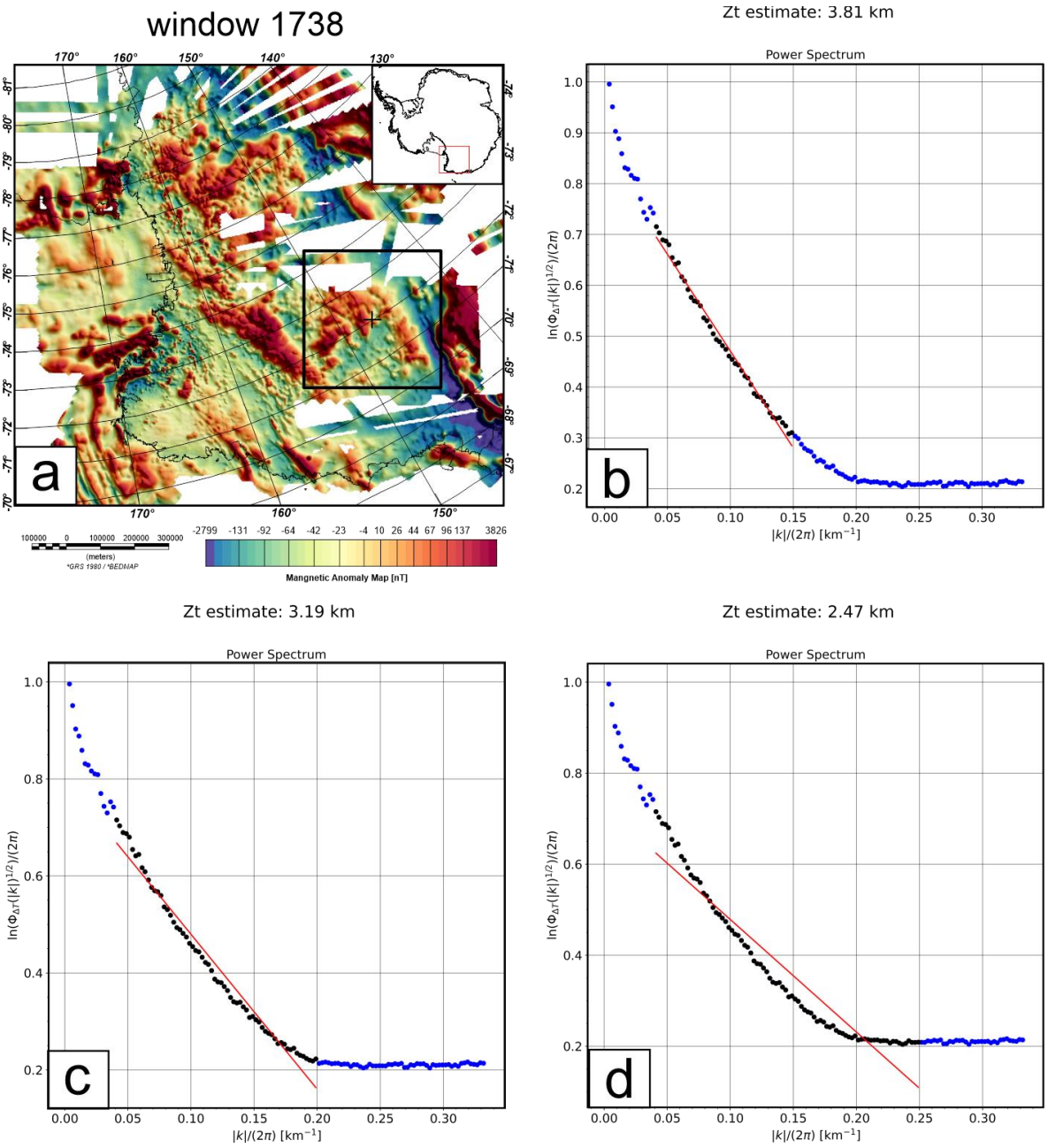

Figure S9. Power spectrum from window 1738 with a window size of 400 km. Blue dots power spectrum data points. Black dots indicate data points used for the linear regression. Red line linear fit to estimate Z0. a) Window location and extent superimposed on magnetic data. b)

wavenumber range 0.04 – 0.25 |k|/2π, Zt estimate: 3.81 km. c) wavenumber range 0.04 – 0.2 |k|/2π, Zt estimate: 3.19 km d) wavenumber range 0.04 – 0.15 |k|/2π, Zt estimate: 2.47 km.

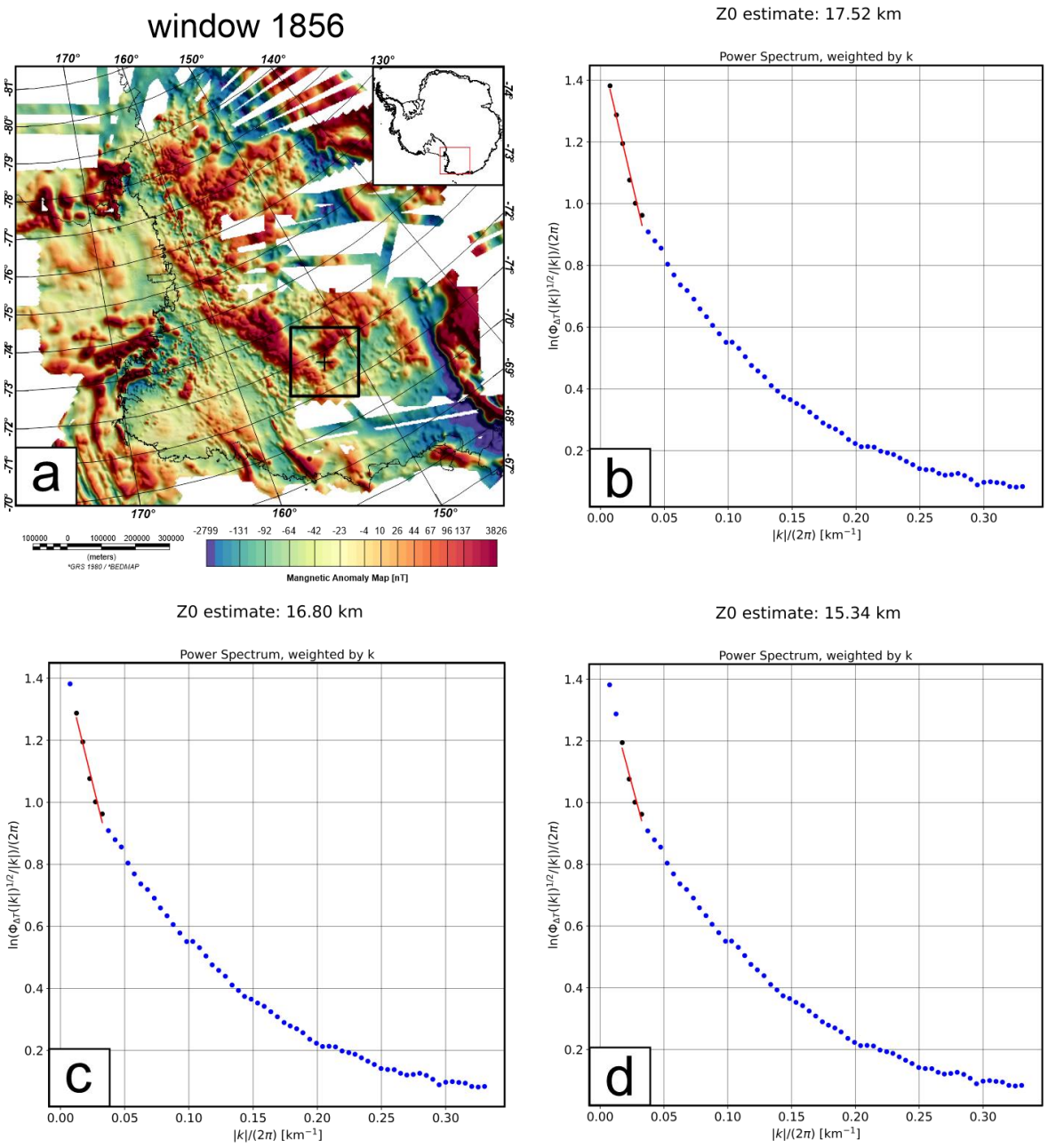

Figure S10. Power spectrum from window 1730 with a window size of 200 km. Blue dots power spectrum data points. Black dots indicate data points used for the linear regression. Red line linear fit to estimate Z0 a) Window location and extent superimposed on magnetic data. b) wavenumber range 0 – 0.033 |k|/2π, Z0 estimate: 17.52 km. c) wavenumber range wavenumber

range 0.01 – 0.033 |k|/2π, Z0 estimate: 16.8 km. d) wavenumber range 0.015 – 0.033 |k|/2π, Z0 estimate: 15.34 km.

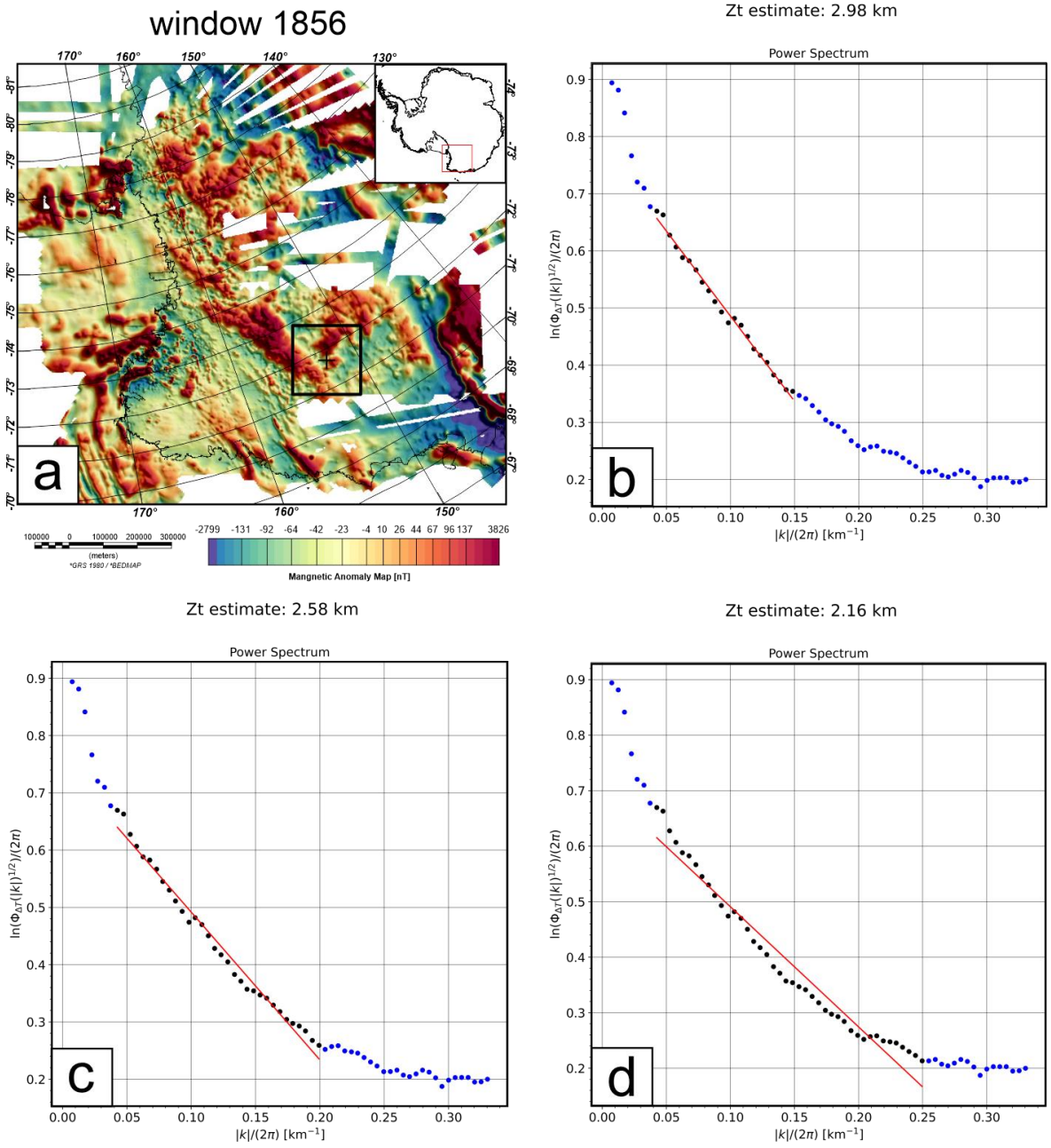

Figure S11. Power spectrum from window 1738 with a window size of 200 km. Blue dots power spectrum data points. Black dots indicate data points used for the linear regression. Red line linear fit to estimate Z_0. a) Window location and extent superimposed on magnetic data. b) wavenumber range 0.04 – 0.25 |k|/2π, Z_t estimate: 2.98 km. c) wavenumber range

0.04 – 0.2 |k|/2π, Z_t estimate: 2.58km d) wavenumber range 0.04 – 0.15 |k|/2π, Z_t estimate: 2.16 km.

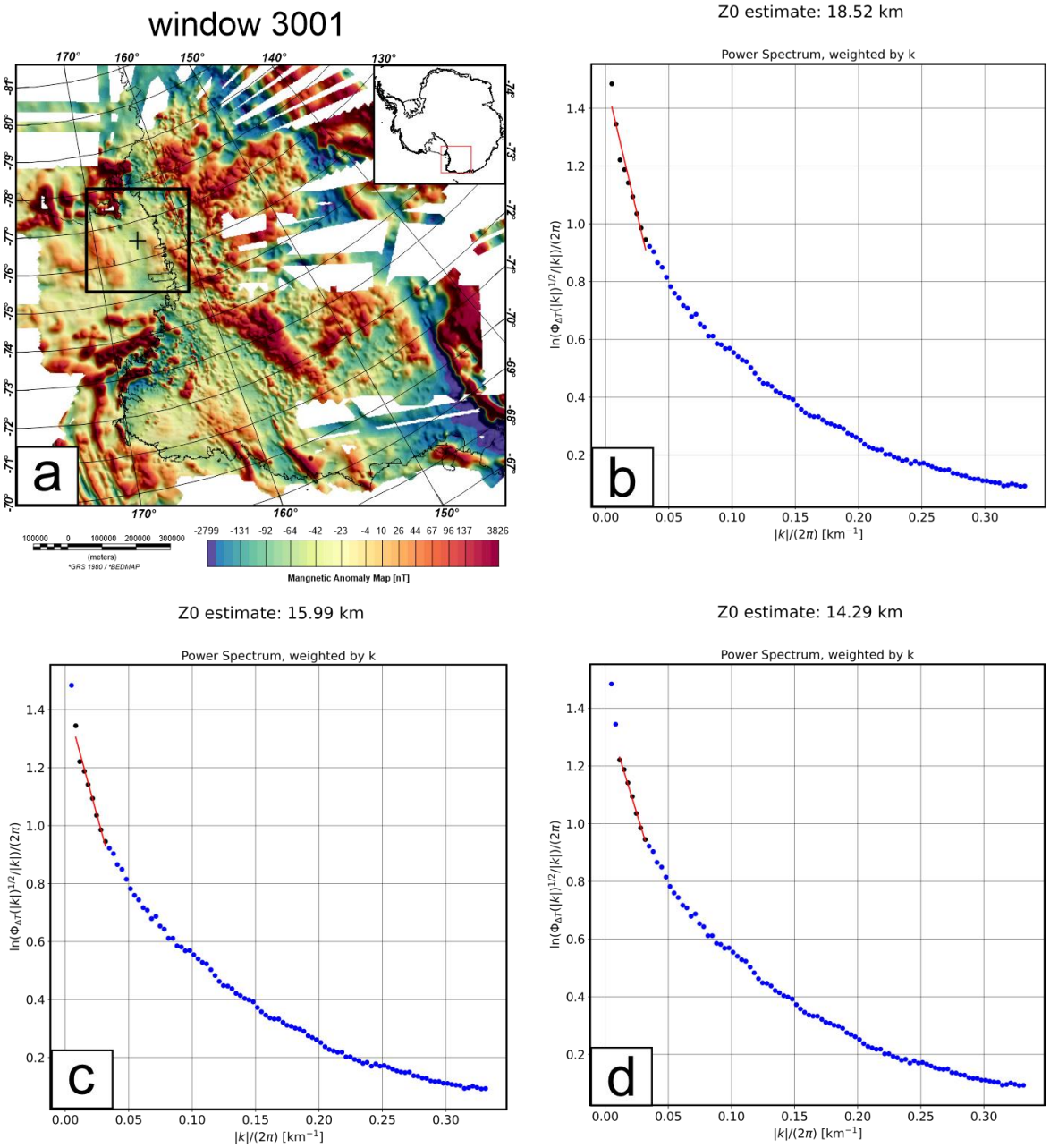

Figure S12. Power spectrum from window 3001 with a window size of 300 km. Blue dots power spectrum data points. Black dots indicate data points used for the linear regression. Red line linear fit to estimate Z0 a) Window location and extent superimposed on magnetic data. b) wavenumber range 0 – 0.033 |k|/2π, Z0 estimate: 18.52 km. c) wavenumber range

wavenumber range 0.006 – 0.033 |k|/2π, Z0 estimate: 15.99 km. d) wavenumber range 0.01 – 0.033 |k|/2π, Z0 estimate: 14.29 km.

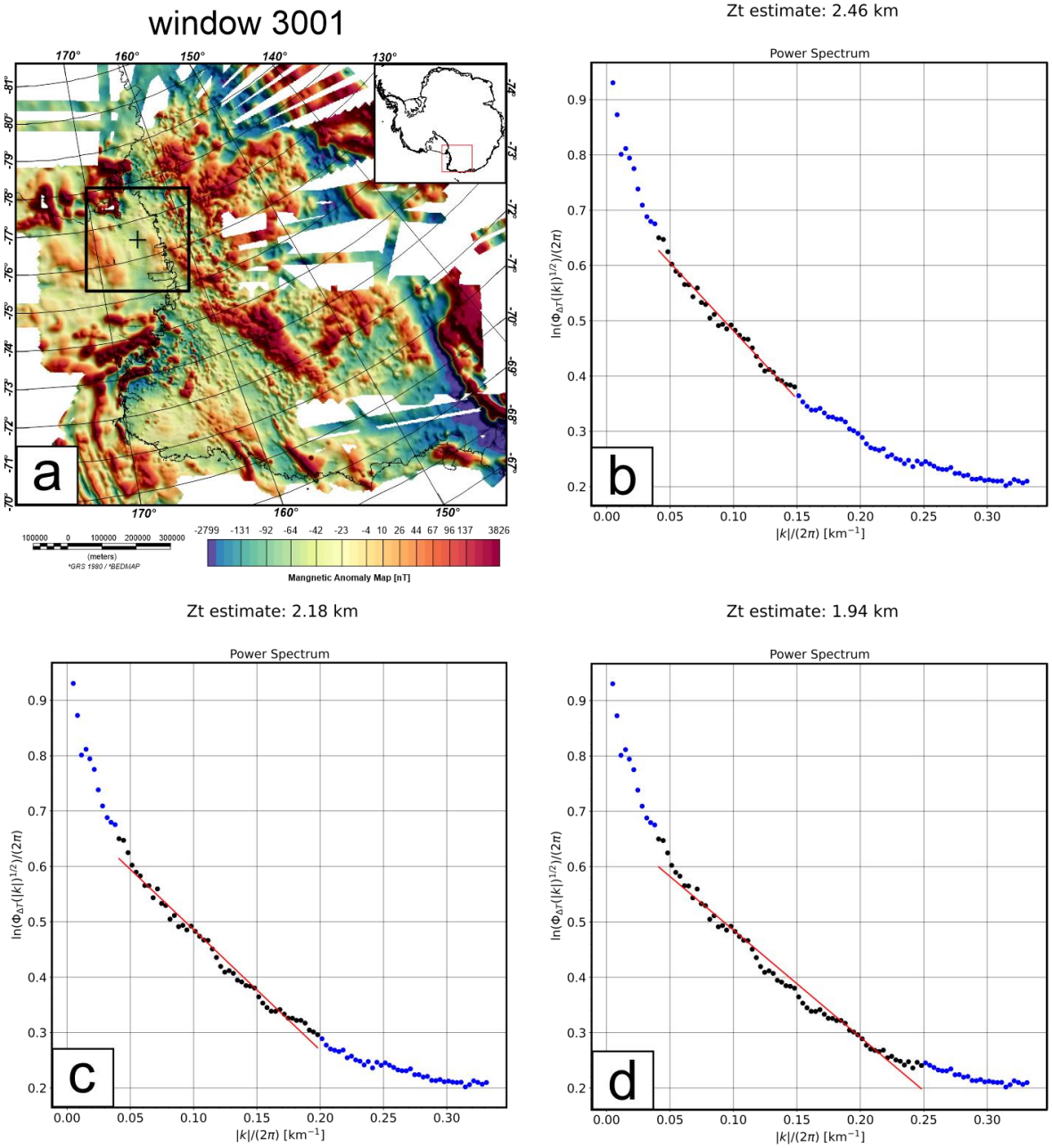

Figure S13. Power spectrum from window 1738 with a window size of 300 km. Blue dots power spectrum data points. Black dots indicate data points used for the linear regression. Red line linear fit to estimate Z0. a) Window location and extent superimposed on magnetic data. b) wavenumber range 0.04 – 0.25 |k|/2π, Zt estimate: 2.46 km. c) wavenumber range 0.04 – 0.2 |k|/2π, Zt estimate: 2.18 km d) wavenumber range 0.04 – 0.15 |k|/2π, Zt estimate: 1.94 km.